Science
AAAS

Supplementary Materials for

Rapid volcanic ash entombment reveals the 3D anatomy of Cambrian trilobites

Abderrazak El Albani *et al*.

Corresponding authors: Abderrazak El Albani, abder.albani@univ-poitiers.fr; John R. Paterson, jpater20@une.edu.au

Science **384**, 1429 (2024)
DOI: 10.1126/science.adl4540

The PDF file includes:

Other Supplementary Material for this manuscript includes the following:

Materials and Methods

Samples and provenance

Four trilobite specimens, in addition to petrological and geochemical samples (table S1), were recovered from the pyroclastic layer in the uppermost Tatelt Formation (Cambrian Series 2, Stage 4; upper *Hupeolenus*–lower *Morocconus notabilis* zones), east of Ait Youb in the Lemdad Syncline, High Atlas Mountains, Morocco. The specimens of *Gigoutella mauretanica* (AY-TA-TB-01 [= MHNM-HA-TT-CA-1A (*22*)] and AY-TA-TB-02) and *Protolenus* (*Hupeolenus*) sp. (AY-TA-TB-03 and AY-TA-TB-04) are primarily preserved as external molds within the ash layer. AY-TA-TB-01 was collected in 2015 by a field party led by A. Azizi, while the other three specimens were collected by a team led by A. El Albani during different fieldtrips conducted since 2021.The trilobite specimens are housed at the Museum of the Department of Energy and Mines, Rabat, Morocco.

X-Ray Microtomography

The µCT analysis of the four trilobite specimens was performed on RX-solutions (Chavanod, France) EasyTom XL Duo equipment with a microfocus X-ray source (Hamamatsu L12161-07), coupled with a flat panel imager (Varian PaxScan 2520 DX). Acquisition parameters were adapted to each sample. AY-TA-TB-01: 130 kV (tube voltage), 70 µA (current), 4320 projections on 3 turns, 2.8 frames per second, 15 frames averaging, 8.8 µm of resolution. AY-TA-TB-02: 140 kV, 71 µA, 4032 projections on 2 turns, 6.6 frames per second, 20 frames averaging, 13.0 µm of resolution. AY-TA-TB-03 (sample divided in two blocs scanned with same parameters) : 140 kV, 71 µA, 1760 projections, 2.8 frames per second, 15 frames averaging, final resolution of 10 µm (after merging). AY-TA-TB-04: 140 kV, 55 µA, 1792 projections, 2.5 frames per second, 15 frames averaging, 8.0 µm of resolution. Slice reconstructions were done with XAct software (RX-Solutions) with a filtered back projection algorithm, attenuation of beam hardening and scattering artefacts, corrections of x-ray spot drift and ring artefacts. Merging with landmarks and rigid transformations (AY-TA-TB-03), semi-automatic (combination of thresholding by boundary, top-hat filter and watershed algorithm) and manual segmentations, virtual sections, 3D surface and volume rendering, and videos were performed with Avizo v. 2022.2 (Thermo Fisher Scientific-FEI). Segmented surfaces of AY-TA-TB-02 appendages have been smoothed with MeshMixer v3.5 (Autodesk).

Optical and Scanning Electron Microscopy

Polished thin sections were studied using a standard optical microscope for detailed examination of textural relationships and mineralogical composition. Thin sections were examined under plane and cross-polarized transmitted light and reflected light using a Nikon ECLIPSE E600 POL microscope attached to a Nikon Digital Sight DS-U1 camera and operated by NIS-Element D software for scanning observations at the University of Poitiers, France. Representative carbon-coated thin sections were examined using a JEOL JSM IT500 scanning electron microscope (SEM) coupled with a Bruker Lynxeye energy dispersive X-ray spectrometer (EDS) and an XFlash 4030 Silicon drift detector at the University of Poitiers, and with an FEI Quanta 200 SEM equipped with an EDS at the University of Lille. The selected polished samples and thin sections were observed in secondary electron (SE) and back-scattered electron (BSE) imaging modes. The semi-quantitative chemical analysis using EDS was performed on an analytical area of ~2 µm at 15 kV accelerating volts, 1 nA beam current, and a working distance of 11 mm. Samples were examined at varying resolutions and magnifications

to provide the finest morphological details, textural relationships, and mineral chemistry obtained through the EDS.

X-Ray Diffraction

Mineralogical composition of the selected bulk rocks and clay fractions (<2 μm) was measured using a Bruker D8 ADVANCE diffractometer with CuKα radiation operated at 40 kV, 40 mA, and 0.025/s step size at the University of Poitiers. Samples for XRD analysis were prepared following standard methods (*61, 62*). The bulk rock powders were scanned between 2–65° 2θ angular range at a step size of 0.025° 2θ per 3 s. The clay-size fractions were dispersed in osmose-purified water using Elma S60 ultrasonic agitation to liberate the fine particles. These fine particles were separated by centrifugation methods using a Sorvall LEGEND XRF centrifuge with a rotating speed of 1000 rpm for 2 min 30 s at 20°C. The obtained <2 μm fractions were pipetted on glass slides and air-dried (AD) to be analysed at room temperature. After AD analysis, the oriented slides were analysed after ethylene-glycol (EG) saturation, and after heating to 350°C and 550°C for 4 hours. The clay fractions were analysed between 2–30° 2θ angular range and a step size of 0.02° 2θ per 3 s. Identification of mineral phases and indexing patterns were obtained using X'pert High Score software through comparison with the international Center for Diffraction Data (ICDD JCPDS PDF3) files and reference data (*61, 62*).

Whole-rock Geochemical Analysis

Whole-rock geochemical analyses of major and trace elements, including rare earth elements, were performed on 46 samples (table S1) at the *Service d'Analyse des Roches et des Mineraux (SARM) of the Centre des Recherches Pétrographiques et Géochimiques (CRPG)*, Nancy, France, using their internal protocols. Approximately 200 mg of powdered sample was fused with lithium metaborate ($LiBO_2$) and dissolved in nitric acid. Major element contents were measured by inductively coupled plasma atomic emission spectrometry (ICP-OES Icp 6500 radial, Thermo-Scientific). Trace elements, including REE concentrations, were measured using inductively coupled plasma mass spectrometry (ICP-MS Icap-Q, Thermo-Scientific), except for Sc (ICP-OES Icp 6500 radial, Thermo-Scientific). Trace-metal concentrations are given in the form EF, where $X_{EF} = [(X/Al)_{sample}/(X/Al)_{PAAS}]$, X and Al stand for the concentrations of element and Al, respectively. If X_{EF} is >1, then the element is enriched, and if X_{EF} is <1, it is depleted relative to average shales, respectively (*63*).

Supplementary Text

Geological setting and age of the Tatelt Formation

The High Atlas Mountains of Morocco extend along the northern margin of the West African Craton. They are bounded by the Variscan domain of Meseta to the north and the Anti-Atlas Mountain to the south. During late Ediacaran to Cambrian times, the Anti-Atlas and High Atlas domains experienced multi-phase rifting, volcanic activity, and multiple episodes of transgression and regression (*64–67*); Geyer and Landing (*64*) provided detailed documentation of the stratigraphic framework, in addition to the palaeogeographic distributions of the thick volcano-sedimentary successions. This study focused on two lithostratigraphic units in the Lemdad Syncline that preserve lower Cambrian strata, namely the Issafen Formation and overlying Tatelt Formation immediately to the east of Ait Youb in the Lemdad Syncline (figs. S1 and S2). Both units belong to the Tata Group, which forms a widespread succession in the Anti-Atlas and the central High Atlas.

The Tatelt Formation and correlative strata (i.e., Asrir Formation) occur in the Anti-Atlas and High Atlas. In the Lemdad Syncline, including the studied section, the Tatelt Formation is up to 12 m thick and forms a sheet-like unit dominated by thick-bedded sandstones (fig. S1). Volcanic activity was prevalent at the time of deposition, and volcanic centers are assumed to be located in the western or north-western High Atlas (*64*). The sandstone beds consist of medium- to fine-grained hummocky cross-stratified feldspar-rich to lithic sandstone, and medium- to coarse-grained trough cross-bedded lithic sandstone with pebbly layers dominated by volcanic clasts. Layers of cream- to white-coloured, fine-grained volcanic ash are recognized by mineral content and texture (fig. S2). A few thin interbeds of green to grey mudstone are also preserved within these amalgamated sandstones.

The Tatelt Formation shows evidence of a sediment provenance derived largely from reworked volcanic and pyroclastic products. In the vicinity of Lemdad, post-Ediacaran volcanism in the High Atlas resulted from early Cambrian rifting involving the Anti-Atlas, High Atlas and Mesetian domains (*66, 67*). This volcanic activity was both effusive and explosive, and volcanoclastic materials were reworked and deposited in the lower Cambrian succession, including the Tatelt Formation.

Above the Tatelt Formation lies the Jbel Wawrmast Formation, which is up to 300 m thick in some areas that experienced pronounced subsidence. Fine-grained deposits of green to yellowish shales with intervening thin beds of fine-grained sandstones, siltstones, and limestones dominate this unit (*64*). The boundary between the Tatelt and Jbel Wawrmast formations is marked by the basal Brèche à *Micmacca* (or "*Micmacca* Breccia") Member within the latter unit – a high-energy, fossiliferous, polymictic deposit (*64*).

Trilobites documented from several sections through the Tatelt Formation in the Lemdad Syncline equate to the *Sectigena*, *Hupeolenus*, *Morocconus notabilis*, and lowermost *Ornamentaspis frequens* zones, ranging from Cambrian Stage 4 to the Wuliuan (*64, 68*). The co-occurrence of *Protolenus* (*Hupeolenus*) sp. and *Gigoutella mauretanica* from the uppermost Tatelt Formation at the studied section is suggestive of an age equivalent to the upper *Hupeolenus*–lower *Morocconus notabilis* zones (Cambrian Series 2, Stage 4) (*64, 68–71*).

No absolute age constraints are available from the basaltic ash that hosts the exceptionally preserved fossils, as it does not contain zircons or other suitable mineral crystals for radiometric dating.

Sedimentological and lithological characteristics

The measured section encompasses the upper part of the Issafen Formation and the overlying Tatelt Formation (figs. S1D and S2). In the Issafen Formation, hummocky cross-bedded sandstones are variably fine- and coarse-grained and range from grey to green in colour. Some lithic-rich epiclastic sandstones contain rounded volcanic pebbles up to a few centimeters in size. Occasionally, shale interbeds in the middle and upper parts contain thin limestone beds with shelly fossils, including brachiopods and trilobites, which can be abundant. Trace fossils of *Cruziana*- and *Planolites*-type are occasionally present. Scour structures are preserved on the bases of several sandstone beds, whereas some upper bedding surfaces are wave-rippled and preserve wide hummocks. Textural and mineralogical features of the hummocky cross-bedded sandstones include: (i) the occurrence of laminae containing abundant feldspars or volcanic clasts, and (ii) erosional lower bounding surfaces up to 10 cm deep, overlain by millimeter-size (4–10 mm) rip-up clasts and pebbles, predominantly of volcanic origin.

The Tatelt Formation at the studied section consists of the following facies: (i) hummocky cross-bedded, fine- to medium-grained sandstone forming meter-thick layers in the lower and middle parts of the formation; the sandstones show the same features observed in the underlying Issafen Formation, but coarse-grained microconglomeratic layers with abundant volcanic clasts are common. (ii) Planar-stratified litharenites forming beds with sharp lower boundaries and wave-rippled upper bedding surfaces. (iii) Meter-thick trough cross-bedded, medium- to coarse-grained litharenites with erosional lower boundaries; thick cosets of this facies are draped by millimeter- to centimeter-thick, grey to yellowish fine-grained ash. Coarse-grained microconglomeratic layers are common—dominated by volcanolithic clasts represented by rounded to subangular pebbles—and cut into the underlying cross-bed sets. Some of these microconglomerates are partially compacted and the remaining voids are filled with fine grained matrix and/or cement. Few bioclasts, primarily brachiopods, are present in the topmost layers.

The pyroclastic layer hosting the exceptionally-preserved fossils lies at the top of the Tatelt Formation (fig. S2). This grey to green-coloured layer, up to 30 cm thick, is comprised of distinct lower and upper parts (fig. S2A). The lower part consists of a welded, coarse-grained, lithic-rich tuff and fine-grained lapillistone with clasts up to 4 mm in size (Fig. 1, A and B, and fig. S2B). The volcanic clasts are dominated by flattened, plastically-deformed microlithic fragments. In portions of the bed with no matrix, the lapilli are highly compacted and welded with irregular contacts (fig. S2B). In parts containing fine-grained matrix, a typical eutaxitic fabric is observed with sigmoidally-deformed and flattened clasts (fig. S2E). Small, scattered, non-deformed clasts with microlitic textures and vesicles typical of scoria are also present. Some clasts are almost entirely replaced by void-filling black calcite. The upper part of the bed consists of grey, very fine-grained volcanic ash, up to 5 cm thick, with sparse grains of plagioclase floating in the ash matrix (fig. S2, A and C); the trilobites documented herein occur in this upper, fine-grained portion of the bed (fig. S2D). The boundary between the lapilli-rich lower layer and the overlying ash-rich layer is sharp, although some isolated lapilli float within the ash matrix along this boundary (Fig. 1, A and B, and fig. S2F).

The contact between the Tatelt Formation and the overlying Jbel Wawrmast Formation is an erosional unconformity, interpreted as a sequence boundary between the aggrading Tatelt Formation sandstones and the transgressive "*Micmacca* Breccia" Member at the base of the Jbel Wawrmast Formation. The boundary indicates an abrupt change in facies and depositional setting. This regional unconformity has been attributed to either epeirogenic or extensional tectonic activity (*20, 72*). The "*Micmacca* Breccia" Member is coarse-grained, with a mixture of

epiclastic and bioclastic sediments, including brachiopods, echinoderms, molluscs and trilobites (*64*), together with significant reworked material. The overlying fine-grained grey shales, typical of offshore facies within the Jbel Wawrmast Formation, contain layers rich in carbonate nodules and concretions up to 1 m in size. These may be fossil-rich and include trilobites, brachiopods and other bioclasts (*64*).

Palaeoenvironmental setting of the Tatelt Formation

The sedimentological features and facies trends across the Issafen and Tatelt formations in the measured section provide insight into the palaeoenvironmental conditions of the High Atlas region during the latest early Cambrian (Series 2, Stage 4). The sequential stacking pattern of facies and the lack of obvious unconformities indicates continuous sedimentation across the Issafen-Tatelt succession; this is also supported by trilobite biozonation (*64*). Overall, the siliciclastic deposits of the upper Issafen Formation and Tatelt Formation are indicative of a shallow marine, storm- and wave-dominated shoreface to foreshore setting. Facies trends indicate a shallowing upward succession, with a transition from lower shoreface deposits (upper Issafen Formation) characterized by interbedded hummocky cross-stratified sandstones and shales, to upper shoreface–foreshore deposits (Tatelt Formation) comprising thick and amalgamated hummocky and trough cross-stratified sandstones. The prograding and subsequent aggrading trends, plus the high amount of epiclastic material provided to the platform, could indicate the presence of a deltaic system delivering volcaniclastic sediments from neighbouring volcanic centers. There is also evidence for sand ridges that were parallel to the shoreline, formed under wave and storm influence. Syn-sedimentary volcanic activity is well documented in the Issafen and Tatelt formations, with several feldspar-rich ash beds recognised (*64*). Most sandstone beds contain large amounts of sodium-rich feldspar, and chlorite and albite are also dominant throughout the section. The XRD data shows a vertical change in chlorite behaviour, with relatively similar 001 and 002 peaks in the lower beds, and then a shift to higher 002 peaks in the upper layers (Fig. 1, D and E). This shift in peaks suggests a change in composition from clinochlore, the Mg-rich member, to chamosite, a more Fe-rich member; this evolution could also indicate a change in oceanic environment (e.g. ferruginous pore-water conditions).

Direct evidence for syn-sedimentary volcanic activity is provided by the pyroclastic flow that occurs at the top of the Tatelt Formation, which contains the trilobites documented herein. All features of this pyroclastic flow indicate material hot enough to produce welded and eutaxitic textures, together with soft deformation of lithic volcanic clasts (fig. S2, B and E). The coarse-grained lapillistone constitutes the lower portion of the pyroclastic flow that sharply grades into a fine-grained ash layer containing the fossils (Fig. 1, A and B, and fig. S2A). The thickness of the pyroclastic layer and the sharp contact with the underlying lithic sandstone indicate that this pyroclastic event was sudden and short-lived. The turbid ash-cloud portion of the flow would have entered the shallow marine setting and quickly buried the trilobites. The rapid remineralization associated with early diagenetic consolidation of the glass-rich ash in seawater prevented burial compaction and facilitated the exceptional preservation of soft tissues prior to decay. This mechanism of preservation constitutes a unique taphonomic circumstance in which organisms were “frozen” in volcanic material delivered to a shallow ocean basin during a sudden pyroclastic event.

Systematic paleontology

Class **Trilobita** Walch, 1771 (*73*)

Order **Redlichiida** Richter, 1932 (*74*)

Suborder **Redlichiina** Richter, 1932 (*74*)

Superfamily **Ellipsocephaloidea** Matthew, 1887 (*75*)

Family **Ellipsocephalidae** Matthew, 1887 (*75*)

Subfamily **Protoleninae** Richter & Richter, 1948 (*76*)

Remarks. Comprehensive studies on the Ellipsocephalidae (*69, 77–80*) have noted the various challenges that exist in dealing with the taxonomy of this family, particularly with regard to subfamilial, generic, and subgeneric concepts. Many of the issues stem from over 100 years of differing views on the phylogeny and classification of ellipsocephalids, in addition to many taxa being described from limited, incomplete and/or poorly preserved material; see Cederström *et al.* (*80*) for an overview. This is particularly true of the diverse Protoleninae, with Geyer & Landing (*78*) stating that members of this subfamily are difficult to identify if specimens are compressed or preserved as internal molds, as is often the case. The Protoleninae and indeed the entire Ellipsocephalidae are in need of revision, with Geyer's (*69*) diagnosis of the family being based on few unambiguous apomorphies, the subfamily likely being paraphyletic, and the genus *Protolenus* itself being diagnosed by ambiguous character states (*77*). Despite these caveats, one of the species represented in the volcanic ash layer in the uppermost Tatelt Formation fits within Geyer's (*69*) concepts of the subfamily, genus *Protolenus* Matthew, 1892, and subgenus *Hupeolenus* Geyer, 1990, so are followed herein.

Genus ***Protolenus*** Matthew, 1892 (*81*)

Type species. *Protolenus elegans* Matthew, 1892; Hanford Brook Formation (Cambrian Series 2, Stage 4), New Brunswick, Canada.

Subgenus ***Hupeolenus*** Geyer, 1990 (*69*)

Type species. *Protolenus* (*Hupeolenus*) *hupei* Geyer, 1990; Tatelt Formation (Cambrian Series 2, Stage 4), Lemdad Syncline, High Atlas, Morocco.

***Protolenus* (*Hupeolenus*) sp.**

Figs. 2, A, C and D, 3, A to O, 4, B to I, figs. S3 and S4, and Movies S1 and S2

Material. AY-TA-TB-03: Complete exoskeleton preserving ventral soft-part anatomy, including the labrum, antennae and post-antennal appendages in the cephalon and trunk. AY-TA-TB-04: Partial specimen preserving parts of the dorsal exoskeleton (genal spine and thoracic pleurae) and post-antennal appendages. Both specimens were recovered from the uppermost Tatelt Formation (Cambrian Series 2, Stage 4; upper *Hupeolenus*–lower *Morocconus notabilis* zones), east of Ait Youb in the Lemdad Syncline, High Atlas Mountains, Morocco.

Description of biomineralised exoskeleton. Total preserved sagittal length of exoskeleton is 12.4 mm in the largest, most complete specimen (AY-TA-TB-03); specimen AY-TA-TB-04 has a preserved length of 10.5 mm. Cephalon broad, length (sag.) *ca.* 60% width (tr.) excluding long genal spines; cephalic length (sag.) *ca.* 40% total exoskeletal length. Trunk composed of 15 thoracic segments and a very small pygidium (length *ca.* 5% sagittal length of exoskeleton).

Cranidium is 5.1 mm in length (sag.); subquadrate in outline; moderate convexity (sag., tr.). Anterior margin strongly curved, width (tr.) equal to γ–γ; posterior margin (excluding occipital ring) straight, directed slightly posterolaterally abaxially to intergenal angle, then directed anterolaterally. Anterior sections of facial suture slightly curved and directed forward from γ; posterior sections of facial suture very short. Glabella gently tapering, anterior width (tr.) at estimated midlength of frontal lobe *ca.* 70% width of LO (tr.); frontal lobe rounded; sagittal length of glabella (including LO) *ca.* 80% cranidial length. Axial furrow shallow, narrow (tr.), straight; preglabellar furrow shallow and narrow (sag., exsag.). S1 very weakly impressed, directed slightly anterolaterally abaxially; no other glabellar furrows are discernible. LO of moderate convexity (sag., tr.); length (sag.) *ca.* 25% glabellar length; posterior margin strongly bowed. SO slightly bowed anteriorly, wide (sag., exsag.), of equal depth across furrow. Preglabellar field moderately downsloping, flat (sag.), length (sag.) *ca.* 10% cranidial length. Preocular field moderately downsloping, flat, max. length (exsag.) *ca.* 18% cranidial length (sag.). Anterior border flat, length (sag.) *ca.* 8% cranidial length, with consistent length abaxially; anterior border furrow strongly curved (parallels anterior cranidial margin), more of a change in slope than a distinct furrow. Palpebral lobe well developed, moderately convex (tr.), length (exsag.) *ca.* 33% cranidial length (sag.), width (tr.) increasing posteriorly, max. posterior width (tr.) *ca.* 35% lobe length, anterior tip situated opposite pre-occipital glabellar midlength (sag.), posterior tip situated opposite SO. Eye ridge of low relief and forming a continuation of the palpebral lobe, weakly convex (exsag.), gently curved anteriorly, separated from glabella by axial furrow, width (tr.) *ca.* 65% adjacent glabellar width. Palpebral area width at ε (tr.) *ca.* 55% adjacent glabellar width. Posterolateral projection of fixigena extremely short (tr.), gently downsloping, broadly rounded distally. Posterior border moderately convex (exsag.), slightly expanding abaxially to fulcrum; posterior border furrow obscured in AY-TA-TB-03.

Rostral plate strongly curved, following same curvature as anterior margin of cranidium, moderately convex (sag.); uniform length (sag., exsag.), length *ca.* 10% width (tr.); rostral suture evenly curved; connective sutures strongly curved inwards; posterior margin smooth. Ventral surface with shallow, very narrow (sag., exsag.) furrow developed around midlength (sag., exsag.), extending across entire width (tr.).

Hypostome natant, subtrapezoidal outline excluding anterior wings; sagittal length *ca.* 92% max. width (tr.) across anterior wings. Anterior margin strongly curved anteriorly but recurves laterally and extends onto anterior wings; lateral margins concave inwards, representing long (exsag.) lateral notches that accommodate the antennae; posterior margin smooth and strongly curved posteriorly. Middle body of similar outline to margin of hypostome, subdivided into a large anterior lobe and small posterior lobe by a wide, shallow middle furrow; anterior lobe length (sag.) *ca.* 65% hypostomal length; posterior lobe length (sag.) *ca.* 20% hypostomal length. Lateral and posterior borders of equal width (tr.)/length (sag., exsag.), defined by change in slope with middle body, and subdivided by short (exsag.) longitudinal furrows that extend from posterolateral edges of hypostome to anterolateral margins of posterior lobe of middle body. Posterolateral margin smooth, without spines.

Librigena *ca.* 7 mm in length, including genal spine; width (tr.) along posterior margin *ca.* 22% length (including genal spine); lateral margin moderately curved, continuing evenly onto genal spine; posterior margin straight before strongly curving onto genal spine. Librigenal field flat and extremely narrow (tr.). Eye socle of low dorsoventral elevation. Lateral border flat to weakly convex, slightly raised above genal field, widening (tr.) posteriorly, becoming widest at genal angle, anteriormost dorsal portion of border sharply tapers to a point; lateral and posterior border furrows more of a subtle change in slope than distinct furrows. Posterior border flat to weakly convex, slightly raised above genal field, narrow (tr.), and short (exsag.). Genal spine long, length *ca.* 60% librigenal length (including spine); gently convex (tr.) dorsal and ventral surfaces; moderately tapering posteriorly, with adaxial curvature. Librigenal doublure dimensions equivalent to lateral and posterior librigenal borders on dorsal surface; a sharp ridge starts on the inner anterior surface of the lateral doublure (near the connective suture), becoming more rounded and less pronounced posteriorly towards the genal angle.

Thorax of 15 segments, length (sag.) *ca.* 60% sagittal length of exoskeleton, slightly increasing in width (tr.) from T1 to T3, then strongly decreasing posteriorly. Axial lobe strongly convex (tr.), gently tapered posteriorly; width (tr.) of T15 axial ring *ca.* 35% width of T1 axial ring. Axial furrows straight. Fulcrum consistently positioned around mid-width (tr.) of pleurae. Axial ring width (tr.) *ca.* 35–40% width of pleura, consistent length (sag., exsag.) *ca.* 50% length of entire segment; preannulus has a consistent length (sag., exsag.) subequal to the axial ring; articulating half rings not clearly visible. Pleura horizontal to fulcrum, then strongly downsloping to distal tip; anterior and posterior pleural bands poorly preserved, but appear to be of roughly equal dimensions; pleural furrow extends from axial furrow and terminates just before base of pleural spine. Pleural spines thorn-like, length *ca.* 20% width (tr.) of pleurae. Doublure of thoracic pleurae developed on ventral side of spines.

Pygidium poorly preserved in AY-TA-TB-03; *ca.* 0.6 mm in length (sag.) and 1.3 mm in width (tr.). Axis and pleural regions largely obscured, but there appears to be at least one axial ring and a terminal piece, as observed in other members of the Protoleninae (e.g. Geyer (*69*), pl. 42, fig. 6a, pl. 44, fig. 12, pl. 45, fig. 3). Specimen AY-TA-TB-04 appears to preserve at least 20 trunk appendage pairs (described below), indicating that the pygidium must possess at least five appendage pairs. This discrepancy between the number of dorsal segments and ventral appendages is known in some other trilobites (*10, 82*).

Description of soft-part anatomy. Appendages: Specimen AY-TA-TB-03 preserves at least 22 appendage pairs in total (Figs. 2A and 3). A pair of antennae and four pairs of post-antennal appendages (C1–4) are present on the cephalon (Figs. 3, A to D, and 4B). The incomplete specimen AY-TA-TB-04 shows at least 22 biramous post-antennal appendages, suggesting a total of 25 appendage pairs including the antennae, with 20 biramous appendage pairs in the trunk, each ventral to an associated dorsal tergite (fig. S4, A, B, D, G and H).

The pair of antennae are flagelliform, with the complete antenna on AY-TA-TB-03 totalling about 10 mm in length, slightly less than the total length of the body (Fig. 2A). Each antenna emerges ventrolaterally from the lateral notch of the hypostome (Fig. 4, B, D, G and H). The base of the antenna appears to extend from a region of arthrodial membrane that articulates with the tissue around the side of the hypostome. The most complete antenna curves several times; near the hypostome it is oriented anteroventrally and slightly medially, then its distal part is oriented posterolaterally. The basal articles are three times as wide as they are long, but narrow distally until they are twice as long as they are wide. The length of the articles is fairly consistent

with only slight shortening distally. Bulging in the antenna demarcates the boundaries between articles and represents the distal end of each article, showing that each widens slightly distally.

The first post-antennal cephalic appendage (C1) is represented by a relatively large, broad protopodite and a small, slender flagelliform structure (Fig. 3, E and F), interpreted here as an exopod (ex1) based on its attachment position and similarities to the morphology of C1 in *Gigoutella mauretanica* (fig. S6, E and F). The dorsal margin of the protopodite is strongly curved in its proximal part. (Fig. 3, A, B, E and F). The attachment of the protopodite to the body by arthrodial membrane is more distal from the gnathal edge in comparison with C2 and more posterior appendages. The appendage is rotated so that it is roughly parallel to the lateral edge of the hypostome and labrum, putting it at a 30–40° angle to the axis (Fig. 3, A and D). The protopodite is broad, its height about 35% its width, and curves around the side and posterior of the labrum, becoming thinner adaxially until it terminates in a straight gnathal edge in close association with the mouth (Fig. 3, C and D). The anterior surface of the protopodite is concave so that the appendage sits immediately against the labrum. Many spines appear to extend adaxially from the gnathal edge, although their small size has resulted in infrequent preservation. The exopod is attached to the base of the protopodite on the distal edge, projecting in the opposite direction from the gnathobase. The number of articles in the exopod is difficult to determine, but there may be up to 20. The exopod has a length of 2.1 mm. There are no discernible features which could represent the endopod.

The second post-antennal cephalic appendage (C2) has a large, flat protopodite, a rudimentary endopod (en2), and an exopod (ex2) composed of a proximal lobe bearing setae and a flagelliform distal part (Fig. 3, G and H). The protopodite is slightly larger than in C1, positioned in very close proximity posterior to it and angled in a similar orientation, but at a 60° angle from the axis (Fig. 3, A and D). The protopodite projects the gnathal edge around the posterior of the labrum, with its concave anterior surface accommodating the protopodite of C1. Spines along the gnathal edge are preserved more readily than on C1, although their limits are harder to differentiate, making their exact size and number difficult to determine (Fig. 3G). The endopod is very small, and appears to have three podomeres. The second podomere represents a small, flat, triangular endite, the distal one being much smaller. The exopod is slightly longer than the protopodite width and is attached to the protopodite posterolaterally, positioning it in a similar orientation to the more posterior exopods, despite the differing orientation of the protopodite. The proximal exopod lobe is flap-shaped with a long distal edge that is broadly curved before flaring out slightly toward the distal part. This distal edge bears a row of elongate oblanceolate setae that are circular in cross-section, some almost 40% the length of the proximal exopod lobe and up to 10 times longer than wide. The distal ramus is a short antenniform projection that curves outwards. Four distinct articles appear to make up this part of the exopod.

The third post-antennal cephalic appendage (C3) and all other posterior appendages are distinctly biramous, with a large protopodite, an elongate endopod composed of seven podomeres including a terminal claw, and a bilobate exopod bearing a fringe of setae (Fig. 3, I to O). C3 and all posterior appendages are oriented perpendicular to the axis, and each protopodite has a concave anterior surface to accommodate the one immediately anterior of it, particularly on C3. The protopodites are large and taper adaxially from their base. From C3 to the first thoracic appendage (T1), the portion of the protopodite where the endopod attaches extends ventrally so that the protopodites become increasingly trapezoidal in anterior view (Fig. 3, I, J and L). Protopodites posterior to C3 have three lobes, referred to here as protopodal endites, forming the gnathal edge that become increasingly distinct from each other on posterior appendages (Fig. 3,

L, N and O). Many spines project adaxially from the gnathal edge. They tend to be more numerous and robust on the anterior appendages (e.g. C4 and T1; Fig. 3, J and L), but tend to cluster on the ends of the protopodal endites on more posterior appendages (Fig. 3, N and O). Finer sparse spines are present mostly on the anterior side of the protopodite, along its ventral edge, and on the sides of the endites. All the endopods from C3 posteriorly are composed of seven distinct podomeres including the small terminal claw, with each endopod being roughly twice the dorsoventral height of its associated protopodite. On C3, the podomeres are generally cylindrical, with the distal end being slightly wider (Fig. 3I). The first podomere has a slight bulge in the middle of its medial side and a smaller bulge is present more distally on the second podomere. On appendages posterior to C3, these bulges become increasingly elongate and are positioned towards the middle of the podomere, forming subtriangular endites on the first five podomeres of all thoracic endopods. On posterior thoracic endopods (e.g. T8), the endite on the first podomere lengthens to be equal to the length of the associated podomere (Fig. 3O). From C4 posteriorly, the endites bear clusters of apical spines or spine bristles, with spine length and numbers increasing posteriorly; for example, individual spines on T8 reach lengths equal to half of the associated protopodite width (Fig. 3O). Terminal claws are rarely preserved in detail, but are formed by a large central claw about half the length of the sixth podomere and a pair of smaller spines, one on each side of it. A few smaller spines might also be present, but are difficult to discern in both specimens. The exopods of C3, C4 and all thoracic appendages have two distinct, flap-like lobes, each bearing a row of setae. The proximal lobe is quite consistent in shape and relative size, with a narrow joint at the base of the lateral edge of the protopodite and a distal widening to approximately twice the initial width where it connects to the distal lobe. On C3, the exopod is narrower compared to posterior exopods, as the distal lobe is relatively small on this appendage. The boundary between lobes occurs roughly in line with the base of the endopod. Along the dorsal (outer) edge is a row of robust oblanceolate setae of almost consistent size, until the row ends near the distal lobe where their length (up to 500 μm) decreases quite rapidly distally. The distal exopod lobe is broad and subovate, except on C3 where it is narrower. A thin raised ridge on the posterior surface of the exopod runs near and parallel with the outer margin bearing the setae. A second, sharper raised ridge can be seen along the inner margin from the joint between lobes towards the distal apex. The setae extend along the outer margin, being shorter at the base of the lobe before rapidly lengthening, then decreasing rapidly around the apex until they disappear shortly past it. These setae are slightly longer than the proximal ones but much thinner and more densely packed.

Regions of arthrodial membrane are present at the base of every appendage, particularly from C3 posteriorly (Fig. 3, J, K, L and M). Striations and wrinkles represent folding of the membrane. Oblanceolate setae occur on the dorsal side of the membrane from C4 posteriorly (Fig. 3, J to O). The setae are slightly shorter than those on the proximal exopod lobe.

Sternites: Each pair of post-antennal appendages (except C1) has an associated sternite positioned between them, with each sternite separated by short (sag.) and narrow (tr.) transverse tendinous bars (Figs. 2A, and 4, C, E and F). The first sternite is much shorter than the other sternites, with a length about 30% of its width. Associated with the orientation and small size of the C2 appendages, this sternite has a subtrapezoidal outline with only slightly concave lateral and anterior margins. The ventral surface is distinctly concave posteriorly, producing a shallow medial groove that flattens anteriorly. The C3 sternite and those posterior to it bear the traditional hourglass shape when viewed ventrally. Sagittally each sternite is asymmetrically convex, resulting in a gentle slope on the anterior portion and a steep slope along the posterior margin

(Figs. 2A, 4F, and fig. S3E). The posterior margin of each sternite is curved. The width of the sternites is relatively consistent, with only gradual narrowing starting at around the 12th sternite. Sternite length appears to match that of the associated dorsal tergite. Together, this results in the sternites becoming proportionately wider (tr.) and shorter (sag.) posteriorly.

Labrum: A bulbous structure with up to 17 lobes separated by parallel anteroposterior/ dorsoventral furrows projecting posterior of the hypostome is interpreted here as a labrum (Figs. 3, C and D, and 4, B, H and I). The furrows become more closely spaced abaxially, resulting in narrower lobes. The medial lobe is the widest, making up almost 20% of the total width of the labrum. The labrum anteroventrally grades into smooth soft tissue that attaches to the dorsal doublure of the hypostome (Fig. 4, G and H). The dorsal surface of the labrum forms a flat platform, with its anterior margin leading to a transverse, slit-like mouth opening (Fig. 4I).

Digestive system: In specimen AY-TA-TB-03, the digestive system starts with the slit-like mouth, which leads to a short, narrow oesophagus that connects to a J-shaped crop and a long, narrow intestine that extends to the posteriormost part of the trunk (Fig. 2, C and D). The mouth opening is a wide, posteriorly-directed transverse slit located at the anterior margin of the labrum, with the dorsal platform of the labrum and the cephalic protopodites forming a feeding chamber (Fig. 4, B to I). The mouth opening narrows to an oesophageal passage that is directed anterodorsally at an angle of about 20° from the horizontal until it meets the crop (Fig. 2C, and fig. S3, D and E). The oesophagus attaches to the crop in a position that approximately aligns to the base of the antennae. The J-shaped crop is about half the width of the hypostome, with its ventral portion positioned midway between the hypostome and its dorsal portion (Fig. 2C). The crop bends around and makes contact with the inside surfaces of the anterior regions of the hypostome and glabella. The crop disconnects from the ventral surface of the glabella and immediately attaches to the intestine in a position that aligns with the labrum. A single pair of anterolaterally-directed extensions located near the posterior of the dorsal portion of the crop are interpreted as digestive glands (Fig. 2, C and D). The intestine is a long, narrow tube running from the posterodorsal end of the crop to the end of the trunk. The unusual dorsal position of the intestine is considered to be taphonomic.

Taxonomic remarks. Identification is based largely on the most complete specimen (AY-TA-TB-03); specimen AY-TA-TB-04 is considered conspecific as it has a similar overall size, and the same appendicular, genal spine, and thoracic pleural morphologies. Despite its small size and poorly preserved dorsal exoskeleton, specimen AY-TA-TB-03 closely resembles *Protolenus* (*Hupeolenus*) *hupei* Geyer, 1990, which also occurs in the Tatelt Formation of the Lemdad Syncline (*64, 69*). Cephalic similarities include: a narrow (tr.), anteriorly-tapered glabella with a rounded frontal lobe; an occipital ring that strongly tapers abaxially; a short (sag.) preglabellar area, with preglabellar field *ca.* 10% cranidial length; short (sag., exsag.) anterior cranidial border that is of subequal length to the preglabellar field; confluent eye ridges and palpebral lobes, the latter being more pronounced above the genal field and becoming wider (tr.) posteriorly; palpebral area width at ε (tr.) *ca.* 55–60% adjacent glabellar width; and anteriorly advanced genal spines that are *ca.* 60% total librigenal length, with moderate curvature. Apart from a well-developed occipital furrow, it is difficult to discern any obvious glabellar furrows in specimen AY-TA-TB-03, which are usually conspicuous in *Hupeolenus* species (*69, 83–86*). This may be explained by the etched dorsal (= external) surface of the exoskeleton obscuring such features, and the fact that glabellar furrows of *Protolenus* species (*sensu lato*) tend to be more deeply incised in larger individuals, as well as on internal molds (*77*).

Geyer's (*69*) diagnoses of the Protoleninae and *Protolenus* also included the presence of a parafrontal band, and for *Hupeolenus*, shallow 'diagonal' furrows on the preocular field – features that appear to be lacking in specimen AY-TA-TB-03. Westrop & Landing (*77*) demonstrated that the parafrontal band in *Protolenus elegans* from the Hanford Brook Formation (New Brunswick, Canada) only develops during holaspid ontogeny. Well-preserved specimens of *P. elegans* with a similar-sized cranidium (e.g. Westrop & Landing (*77*), fig. 7.8) to that of specimen AY-TA-TB-03 have relatively lightly impressed glabellar furrows and do not show signs of a parafrontal band, which may explain their absence in AY-TA-TB-03. It should also be noted that some cranidia of *Protolenus* (*Hupeolenus*) *hupei* do not exhibit an obvious parafrontal band (e.g. Geyer (*69*), pl. 46, figs 1–3, 5, 6, 9, 13, 14), or 'diagonal' furrows on the preocular field (e.g. Geyer (*69*), pl. 46, figs 3, 4, 5, 8).

Based on the morphological features discussed above, coupled with stratigraphic occurrence and geographic proximity, it is possible that specimens AY-TA-TB-03 and AY-TA-TB-04 represent small holaspides of *Protolenus* (*Hupeolenus*) *hupei*. However, two other *Protolenus* (*Hupeolenus*) species, *P.* (*H.*) *termierelloides* Geyer, 1990 and *P.* (*H.*) sp. A, have also been documented from the Tatelt Formation in the Lemdad Syncline (*64, 69*). As these taxa share very similar cranidial features to specimen AY-TA-TB-03, we place the limited material documented herein under open nomenclature.

Family **Palaeolenidae** Hupé, 1953 (*87*)

Genus ***Gigoutella*** Hupé, 1953 (*87*)

Type species. *Gigoutella atlasensis* Hupé, 1953; Bréche à *Micmacca* Member, Jbel Wawrmast Formation (Cambrian Series 2, Stage 4), Lemdad Syncline, High Atlas, Morocco.

Gigoutella mauretanica (Ortega-Hernández, Azizi, Hearing, Harvey, Edgecombe, Hafid & El Hariri, 2017)

Figs. 2, B, E and F, 4A, figs. S5 to S9, and Movies S3 and S4

2017 *Xandarella mauretanica* Ortega-Hernández, Azizi, Hearing, Harvey, Edgecombe, Hafid & El Hariri; p. 5, fig. 4.

Material. AY-TA-TB-01 [= MHNM-HA-TT-CA-1A in (*22*)]: Specimen preserving remnants of the hypostome, cephalic doublure and thoracic pleurae, in addition to the labrum, antennae, and post-antennal appendages in the cephalon and trunk. AY-TA-TB-02: Partial exoskeleton preserving ventral soft-part anatomy, including the labrum, antennae and post-antennal appendages in the cephalon and trunk. Both specimens were recovered from the uppermost Tatelt Formation (Cambrian Series 2, Stage 4; upper *Hupeolenus*–lower *Morocconus notabilis* zones), east of Ait Youb in the Lemdad Syncline, High Atlas Mountains, Morocco.

Description of biomineralised exoskeleton. Total preserved length of exoskeleton in specimen AY-TA-TB-02 is *ca.* 26 mm; estimated length of exoskeleton in AY-TA-TB-01 is *ca.* 24 mm. Cephalon broad, length (sag.) *ca.* 55% max. width (tr.). Trunk composed of at least 14 thoracic segments.

Cranidium 10.8 mm in length (sag.); subquadrate in outline; strong convexity (sag., tr.). Anterior margin moderately curved, width (tr.) *ca.* 63% max. cephalic width; posterior margin straight between occipital ring and intergenal angle, then directed anterolaterally a short distance. Anterior sections of facial suture broadly curved, diverging anteriorly between γ and β at *ca.* 80° from each other, then converging between β and α; posterior sections of facial suture short and appear to diverge posterolaterally. Glabella clavate in outline, expanding forward, max. width (tr.) at anterior about 1.3 times width of LO (tr.); frontal lobe broadly rounded; sagittal length (including LO) *ca.* 92% cranidial length. Axial furrow shallow, narrow (tr.), straight; preglabellar furrow shallow and narrow (sag., exsag.). S1 very weakly impressed, directed slightly anterolaterally abaxially; no other glabellar furrows are discernible. LO strongly convex transversely, but flat sagittally; length (sag.) *ca.* 20% glabellar length; posterior margin strongly bowed. SO straight, narrow (sag., exsag.), of equal depth across furrow. Preglabellar field absent. Preocular field strongly downsloping, moderately convex (exsag.), max. length (exsag.) *ca.* 15% cranidial length (sag.). Anterior border strongly convex, length (sag.) *ca.* 8% cranidial length, slightly expands (exsag.) abaxially; anterior border furrow more of a change in slope than a distinct furrow. Palpebral lobe well developed, reniform, moderately convex (tr.), length (exsag.) *ca.* 35% cranidial length (sag.), max. width (tr.) at midlength *ca.* 30% lobe length, midlength (exsag.) of lobes align approximately with midlength (sag.) of cranidium. Eye ridge of low relief and forming a continuation of the palpebral lobe, weakly convex (exsag.), almost straight, separated from glabella by axial furrow, width (tr.) *ca.* 40% adjacent glabellar width. Palpebral area width at ε (tr.) *ca.* 60% adjacent glabellar width. Posterolateral projection of fixigena short (tr.), gently downsloping. Posterior border moderately convex (exsag.), slightly expanding abaxially to fulcrum; posterior border furrow expands abaxially.

Rostral plate moderately curved, following same curvature as anterior margin of cranidium, strongly convex (sag.); length (sag.) *ca.* 6% width (tr.), expands (exsag.) abaxially; rostral suture evenly curved; connective sutures strongly curved inwards; posterior margin smooth. Ventral surface with sharp ridge developed around midlength (sag., exsag.), extending across entire width (tr.).

Hypostome natant, subrectangular outline excluding anterior wings; sagittal length *ca.* 1.05 times max. width (tr.) across small anterior wings. Anterior margin smooth, strongly curved anteriorly; lateral margins with short (exsag.) lateral notches that accommodate the antennae; posterolateral margins with three pairs of small spines; posteromedial margin smooth and slightly curved posteriorly. Middle body of similar outline to margin of hypostome, subdivided into a large anterior lobe and small posterior lobe by a wide, shallow middle furrow; anterior lobe length (sag.) *ca.* 70% hypostomal length; posterior lobe length (sag.) *ca.* 12% hypostomal length. Lateral and posterior borders of equal width (tr.)/length (sag., exsag.), defined by change in slope with middle body.

Librigena *ca.* 9 mm preserved length, including broken genal spine; lateral margin moderately curved, continuing evenly onto genal spine; posterior margin straight before strongly curving onto genal spine. Librigenal field moderately convex and strongly downsloping. Eye socle of low dorsoventral elevation. Lateral border strongly convex, slightly widening (tr.) posteriorly, becoming widest at genal angle, anteriormost dorsal portion of border sharply tapers to a point; lateral and posterior border furrows more of a subtle change in slope than distinct furrows. Posterior border moderately convex, slightly raised above genal field, narrow (tr.), and short (exsag.). Genal spine strongly convex (tr.) dorsal and ventral surfaces; moderately tapering posteriorly. Librigenal doublure dimensions equivalent to lateral and posterior librigenal borders

on dorsal surface; sharp ridge on rostral plate continues onto lateral librigenal doublure, becoming less pronounced posteriorly before disappearing near genal angle.

Thorax of at least 14 segments. Fulcrum positioned around mid-width (tr.) of pleurae. Pleura horizontal to fulcrum, then strongly downsloping to distal end; anterior pleural band expands abaxially with well-developed facet; posterior pleural band tapers abaxially; deep pleural furrows extend from axial furrow and terminate just before base of pleural spines. Pleural spines spatulate; T2 macrospinous, with the spine being at least twice the length of other pleural spines. Doublure of thoracic pleurae developed on ventral side of spines.

Pygidium unknown.

Description of soft-part anatomy. Appendages: A pair of uniramous antennae and at least 23 pairs of biramous appendages are present in *Gigoutella mauretanica* (Fig. 2B, and fig. S8A). The cephalon bears the antennae as well as four pairs of post-antennal appendages (C1–4), leaving at least 18 trunk appendage pairs (figs. S6 and S7).

Antennae are flagellifom with neither specimen preserving a complete antenna; the longest partial antenna from AY-TA-TB-01 equals a third of the total body length (fig. S8A). Arthrodial membrane connects the antennae to the body at the lateral notch of the hypostome (Fig. 4A, and fig. S5E). The arthrodial membrane curves so that the base of each antenna is projected anteroventrally (Fig. 4A, and fig. S8A). Individual articles cannot be identified in either specimen.

The first post-antennal cephalic appendage (C1) is mostly composed of a single, wide protopodite bearing a small flagelliform exopod (ex1) and a rudimentary endopod (en1) (fig. S6, E and F). The protopodite is positioned directly posterior to the antenna and slightly curves around it laterally. The gnathal edge of the protopodite is projected around the labrum posterolaterally, near the inferred position of the mouth, and the appendage is oriented 40–50° from the axis (fig. S6C). The dorsal margin of the protopodite is slightly curved in its proximal part, as far as the middle of its width, where the base of the appendage is attached to the body (fig. S6, E and F). The protopodite has a height about 40% its width, is anteroposteriorly flattened and curved, producing a concave anterior surface. Spines with lengths up to $1/8^{th}$ the protopodite width line the gnathal edge. A small projection from the distal edge of the protopodite is interpreted here as the endopod, based on the position of the C3 endopod. The exopod on C1 is flagelliform, of length 1.3 mm. The base of the exopod is broad and flat, becoming more cylindrical distally. The number of segments is unclear.

The second post-antennal cephalic appendage (C2) has similar morphology to C1, but has a lanceolate flap-like exopod with a row of setae along its edge (fig. S6, G and H). Angled at 60° from the axis, the protopodite extends around the labrum posterolaterally, accommodating the protopodite of C1 on the concave anterior side (fig. S6, C and D). Maximum protopodite height is 45% its width. The gnathal edge bears spines arranged in a single row, associated with thin bristle-like spines on the concave anterior surface near the labrum. A short, wide projection at the distal portion of the ventral edge of the protopodite is interpreted here as the endopod, based on the position of the C3 endopod; the limits of the endopod are unclear. The exopod consists of a lanceolate flap-like lobe with a row of large setae and possibly a small antenniform distal projection. The lobe has a broad base where it attaches to the protopodite, its width slightly greater than the maximum height of the protopodite, then tapers to a distal point with a curved outer margin (bearing the setae) and a straight inner margin. The lobe height is about 30% its maximum width. Setae are oblanceolate and circular in cross-section, reaching lengths up to 50%

the medial height of the lobe, although their lengths reduce substantially towards both ends of the lobe. A very small, elongate structure appears to extend from its tip that may represent a small antenniform distal projection, based on similarities to C2 of *Protolenus* (*Hupeolenus*) sp. (Fig. 3H); however, no flexion or articles can be discerned, so this structure could represent a small distal lobe.

The third post-antennal cephalic appendage (C3) and all other posterior appendages are distinctly biramous, with large gnathobasic protopodites, large spinose endopods, and flap-like exopods bearing setae (figs. S6 to S9). Protopodites are large, anteroposteriorly flat, and bear gnathobasic spines. The gnathal edge bears many spines, surrounded by finer bristle-like ones mostly on the anterior surface but also posteriorly and on the ventral margin (figs. S6, I to L, S7, D to F, S8A and S9, A and B). On protopodites of some posterior thoracic segments of AY-TA-TB-01, a small lobe at the distal end of the gnathal edge appears to represent an endite with a less prominent second endite possibly present just before it (fig. S8). The C3 endopod is shorter and more robust than the posterior endopods, being composed of six podomeres, including a terminal claw (figs. S6, D, I and J, and S9, A, D and G). Non-terminal podomeres become more elongate distally on all endopods and exhibit an axially directed endite. The latter change antero-posteriorly from slight extensions to substantial protrusions that are equal in length to the width of the associated podomere. The position of the endite on each podomere shifts from being medial to distal along the length of the endopod. Clusters of elongate spines are present apically on the endites, with some spines reaching lengths equal to the width of their associated podomere; the length and number of spines increase posteriorly. The terminal claws show a single large, curved primary claw, with up to four smaller claws positioned around it (fig. S7, J and M). The terminal claw region is about half the length of the sixth podomere. The exopods are flap-like, posteriorly concave structures composed of two lobes, each with a fringe of setae. The total width is roughly twice the width of the protopodite. The proximal lobe is narrowest at its proximal base, expanding distally to achieve maximum height medially. A raised ridge on the posterior surface extends from the base to the end of the proximal lobe, running parallel with the outer margin bearing the setae (fig. S6, J and L). Elongate oblanceolate setae fringe the outer margin of the proximal lobe, matching the description of those on C2; some setae on the proximal lobe of the thoracic exopods possess up to four apical bristles, each reaching lengths up to 20% of the associated setal length (fig. S9E). The boundary between the proximal and distal lobes is not visible on the C3 and C4 exopods, but can be inferred from the reduction in length (and eventual disappearance) of the large setae on the proximal lobe, suggesting that the distal lobe has a subtriangular outline (fig. S6, I, J, K and L). The proximal lobe of C3 is almost elliptical, narrowing in its distal half, but maintains a greater height than at the base (fig. S6, I and J). The distal lobe of C3 is small, about 20% of the proximal lobe's maximum height. The distal lobe on C4 is much taller and larger, with a maximum width about 85% the width of the proximal lobe. The thoracic distal exopod lobes are wider at their base than the associated proximal lobes (fig. S7, D, E and F). The setae on the distal lobes are infrequently preserved on both specimens, particularly on anterior appendages; they are long and thin, reaching similar lengths to the proximal setae, but generally less than half the width, with similar spacing as the proximal setae.

Sternites: Faint axial subdivisions between the post-antennal appendages are only visible on the holotype (figs. S8 and S9) and are interpreted as sternites separated by transverse tendinous bars. A sternite is present between every pair of distinctly biramous appendages, starting with C3 and ending at T11 (fig. S8A). Preservation does not allow us to see if sternites are present

anteriorly of C3 or after T11. Sternites are represented by simple, ventrally raised regions between the protopodites in the food groove, which runs along the ventromedial part of the thorax and cephalon posterior to the hypostome and labrum.

Labrum: A bulbous structure with up to 13 lobes separated by parallel anteroposterior/ dorsoventral furrows is interpreted here as a labrum (Fig. 4A, and figs. S6, C and D, S8B and S9B). The labrum is positioned posterior to the hypostome, with the main lobate portion grading into smooth soft tissue that attaches the labrum to the dorsal doublure of the posterior margin of the hypostome. The lobes become shorter and narrower laterally. The dorsal surface of the labrum forms a flat platform, which at its anterior margin would be the inferred mouth opening, based on similarities to *Protolenus* (*Hupeolenus*) sp.

Digestive system: Only a part of the digestive system is preserved in specimen AY-TA-TB-02, which most likely represents collapsed portions of the crop (fig. S7, B and C). In ventral view, the crop has four parts separated by distinct boundaries, which could be taphonomic artefacts. There are also anteriorly two smaller lateral nodules and, ventrally, a flat and elongated, almost triangular element, separate from the others.

Taxonomic remarks. Specimen AY-TA-TB-01 was originally documented as the holotype of a new species of *Xandarella*, *X. mauretanica*—a trilobite-like artiopodan (petalopleuran) euarthropod—by Ortega-Hernández *et al.* (*22*), which was collected from the same stratigraphic level and locality as the other Tatelt Formation trilobites described herein. This specimen was described from the external mold that exposes the ventral morphology in negative relief, particularly the antennae, post-antennal appendages, hypostome, and labrum. Microtomographic analysis has revealed these structures in considerably more detail, which are directly comparable to specimen AY-TA-TB-02, especially the spinose margin of the hypostome and identical post-antennal appendages. Although the dorsal exoskeletal features of the holotype are mostly unknown, the course of the cephalic outline, shape of the base of the genal spine, and transverse posterior margin of the hypostome with marginal spines in corresponding positions, together with the appendage details, allow specimen AY-TA-TB-02 to be identified as the same species.

The dorsal exoskeletal morphology of specimen AY-TA-TB-02 is very similar to the palaeolenid *Gigoutella atlasensis* Hupé, 1953 from the Tatelt and Jbel Wawrmast formations in the Lemdad Syncline (Sdzuy (*88*), pl. 1, fig. 7; Geyer (*70*), pl. 1, figs 14–16, 18–22, pl. 3, figs 11–13; Geyer & Landing (*64*), p. 74, 84). Cephalic similarities include: a strongly convex (sag., tr.), anteriorly-expanding, clavate glabella with a broadly rounded frontal lobe; a very short (sag.) to absent preglabellar field; an anterior cranidial border that slightly expands (exsag.) abaxially, extending onto the lateral librigenal border that continues to widen (tr.) posteriorly; short (tr.) eye ridges and long palpebral lobes; and a palpebral area width at ε (tr.) *ca.* 60–65% adjacent glabellar width. The glabella of AY-TA-TB-02 is largely effaced, but there appears to be very faint lateral furrows that correspond to the position of the S1 furrows in *G. atlasensis* (Sdzuy (*88*), pl. 1, fig. 7; Geyer (*70*), pl. 1, figs 14, 16, 18, 22). It is important to note that only exfoliated cranidia of *G. atlasensis* exhibit clear lateral glabellar furrows (e.g. Sdzuy (*88*), pl. 1, fig. 7; Geyer (*70*), pl. 1, fig. 22).

Only a single thoracic segment of *Gigoutella atlasensis* has been previously illustrated (Geyer (*70*), pl. 3, figs 11, 12), but it closely resembles the thoracic pleural features in AY-TA-TB-02, especially the well-developed furrows and the spatulate pleural tips on T8 and T9 (fig. S5D). Specimen AY-TA-TB-02 also exhibits an elongate pleural spine on the second thoracic segment (fig. S5, A, B and D), a feature known to occur in the palaeolenid *Palaeolenus*

longispinus from the early Cambrian Guanshan biota of China (Zhang *et al.* (*89*), pl. 73, figs 11, 12; Luo *et al.* (*90*), pl. 19, figs 1–3).

It is possible that *Gigoutella mauretanica* is a junior subjective synonym of *G. atlasensis*, given their morphologic, stratigraphic and geographic similarities. However, as both species are known from limited material, they should be treated as separate taxa until additional specimens become available. There has also been the suggestion that *Gigoutella* may be a junior synonym of *Palaeolenus* (*91, 92*), but we follow Elicki & Geyer (*93*) in retaining *Gigoutella* as a valid genus until a comprehensive revision of the Palaeolenidae is conducted.

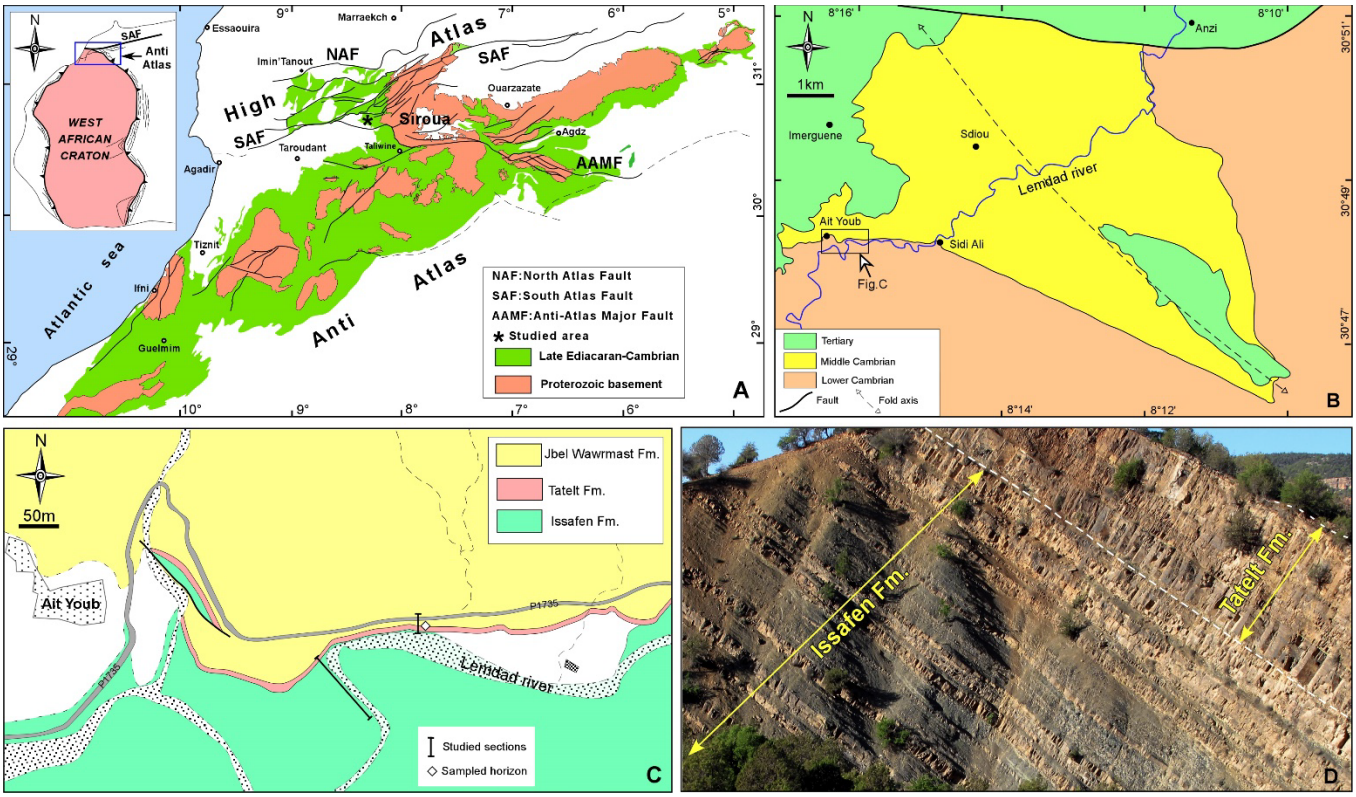

Fig. S1. Geology of the Tatelt Formation, Lemdad Syncline, High Atlas Mountains, Morocco. (**A**) Simplified map showing the occurrence of late Ediacaran–Cambrian strata in the Anti-Atlas and High Atlas Mountains of Morocco, including the location of the study area in the Lemdad Syncline at the western margin of basement exposures in the Siroua area; inset shows the location along the northern margin of the West African Craton. (**B**) Simplified geological map of the Lemdad Syncline and location of the study area, east of Ait Youb. (**C**) Detailed geological map showing the studied sections of the Issafen and Tatelt formations. (**D**) Measured section across the Issafen and Tatelt formations. The upper part of the Issafen Formation consists of interbedded shales and sandstone. The Tatelt Formation consists of thick, sheet-like sandstones, occasionally with thin interbeds of conglomerate and shales. White dashed line indicates the boundary between the two formations.

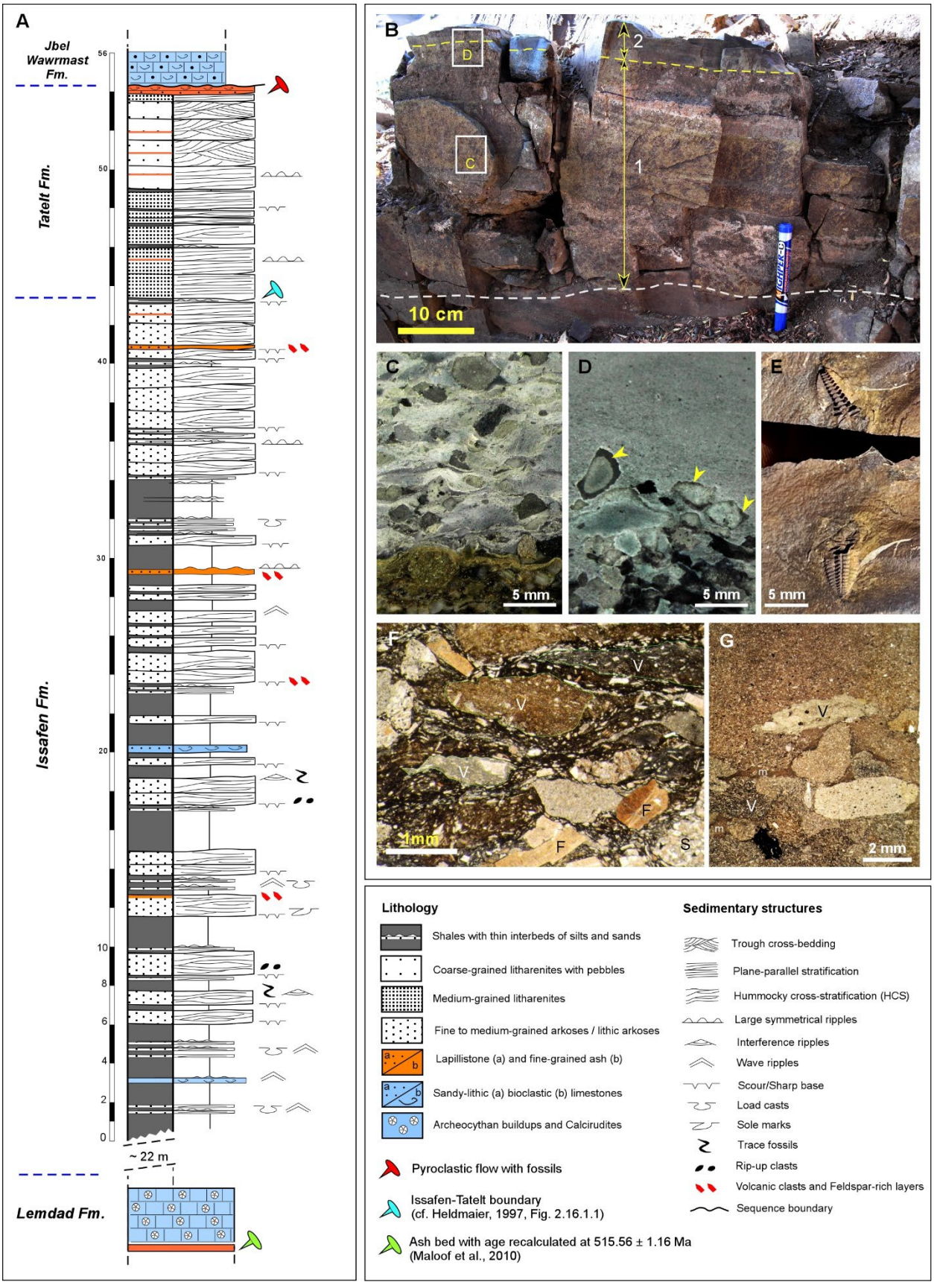
A
Jbel Wawrmast Fm.
Tatelt Fm.
Issafen Fm.
Lemdad Fm.
~ 22 m
B
D
C
2
1
10 cm
C
5 mm
D
5 mm
E
5 mm
F
V
V
V
F
F
S
1mm
G
V
V
m
m
2 mm
Lithology
Shales with thin interbeds of silts and sands
Coarse-grained litharenites with pebbles
Medium-grained litharenites
Fine to medium-grained arkoses / lithic arkoses
Lapillistone (a) and fine-grained ash (b)
Sandy-lithic (a) bioclastic (b) limestones
Archeocythan buildups and Calcirudites
Pyroclastic flow with fossils
Issafen-Tatelt boundary
(cf. Heldmaier, 1997, Fig. 2.16.1.1)
Ash bed with age recalculated at 515.56 ± 1.16 Ma
(Maloof et al., 2010)
Sedimentary structures
Trough cross-bedding
Plane-parallel stratification
Hummocky cross-stratification (HCS)
Large symmetrical ripples
Interference ripples
Wave ripples
Scour/Sharp base
Load casts
Sole marks
Trace fossils
Rip-up clasts
Volcanic clasts and Feldspar-rich layers
Sequence boundary

Fig. S2. Stratigraphy and features of the fossiliferous pyroclastic layer of the Tatelt Formation at the Ait Youb section. (**A**) Stratigraphic log of the section through the upper Issafen and Tatelt formations (as shown in fig. S1D). (**B** to **G**) Detailed features of the studied fossil-bearing pyroclastic layer at the top of the Tatelt Formation. (B) Profile view of the pyroclastic layer showing the thick, coarse-grained lower part (1) rich in lapilli, grading upward to the thin, fine-grained upper part (2) comprised of ash; white dashed line indicates the contact with the underlying lithic sandstone. (C) Polished slab of lapillistone showing the soft deformation during welding around the volcanic clasts, including those composed of microlitic basalt, and alignment typical of eutaxitic texture. (D) Polished slab from the boundary between the lapilli-rich and ash-rich layers, the former showing clasts that are flattened and welded together; note the presence of chilled margins around the juvenile clasts (see arrows). (E) Trilobite specimen AY-TA-TB-03 found within the fine-grained ash layer. (F) Photomicrograph showing the petrographic and textural features of the lapilli-rich layer, including the eutaxitic texture; clasts are dominated by juvenile lithic clasts [V] of volcanic origin, aligned and exhibiting ductile deformation, and isolated feldspars [F] and subordinate sedimentary clasts [S] are also present. (G) Photomicrograph from the boundary of the lapillistone and the fine-grained ash layer; note the sharp transition, the lithic volcanic clasts [V] with microlitic texture, welded and flattened, and the remnant voids filled by fine ash matrix [m].

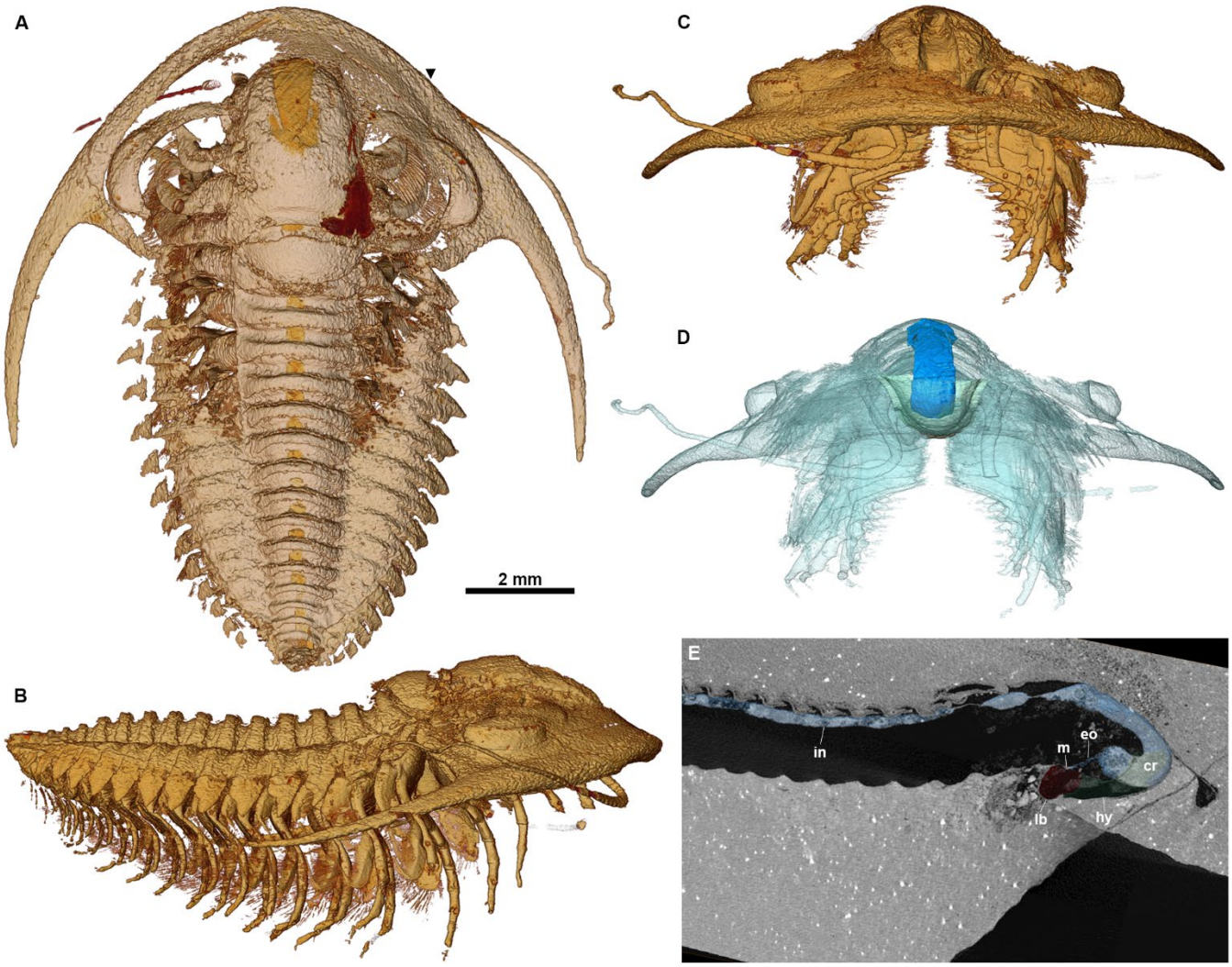

Fig. S3. External morphology and digestive system of *Protolenus* (*Hupeolenus*) sp. (AY-TA-TB-03). (**A** to **D**) Dorsal, lateral and anterior views showing details of dorsal exoskeleton, ventral appendages, hypostome (green), and crop (blue); black arrow in (A) indicates position of anterior facial suture; (D) has surface rendering with transparency, except for the digestive system. (**E**) Single microCT image slice through the sagittal plane of the individual showing details of the ash-filled digestive system (blue), and the position of the hypostome (green) and labrum (red). Scale bar for (A) also applies to (B to E). cr, crop; eo, esophagus; hy, hypostome; in, intestine; lb, labrum; m, mouth.

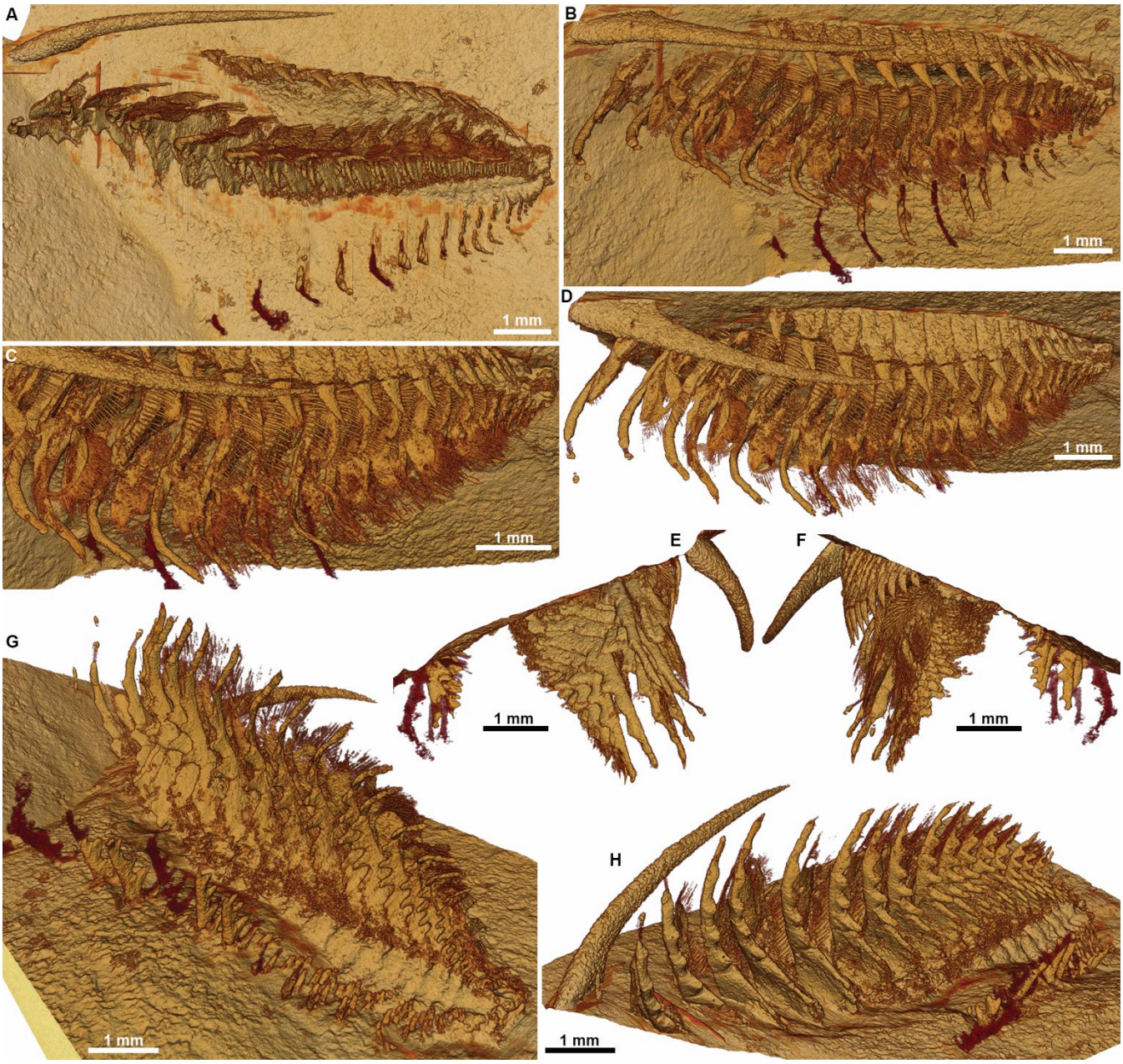

Fig. S4. External morphology of *Protolenus* (*Hupeolenus*) sp. (AY-TA-TB-04). (**A**) Ventral view showing partially exposed genal spine, thoracic pleurae and post-antennal appendages. (**B** to **D**) Oblique lateral views showing details of genal spine, thoracic pleurae, and biramous appendages, including the endopods and exopods with proximal lobes bearing stout oblanceolate setae and distal lobes having slender setae; note etched surface of exoskeleton. (**E** and **F**) Anterior and posterior views, respectively. (**G** and **H**) Oblique postero- and anteroventral views, respectively, showing at least 22 pairs of post-antennal appendages, with endopods displaying endites that become progressively elongate posteriorly.

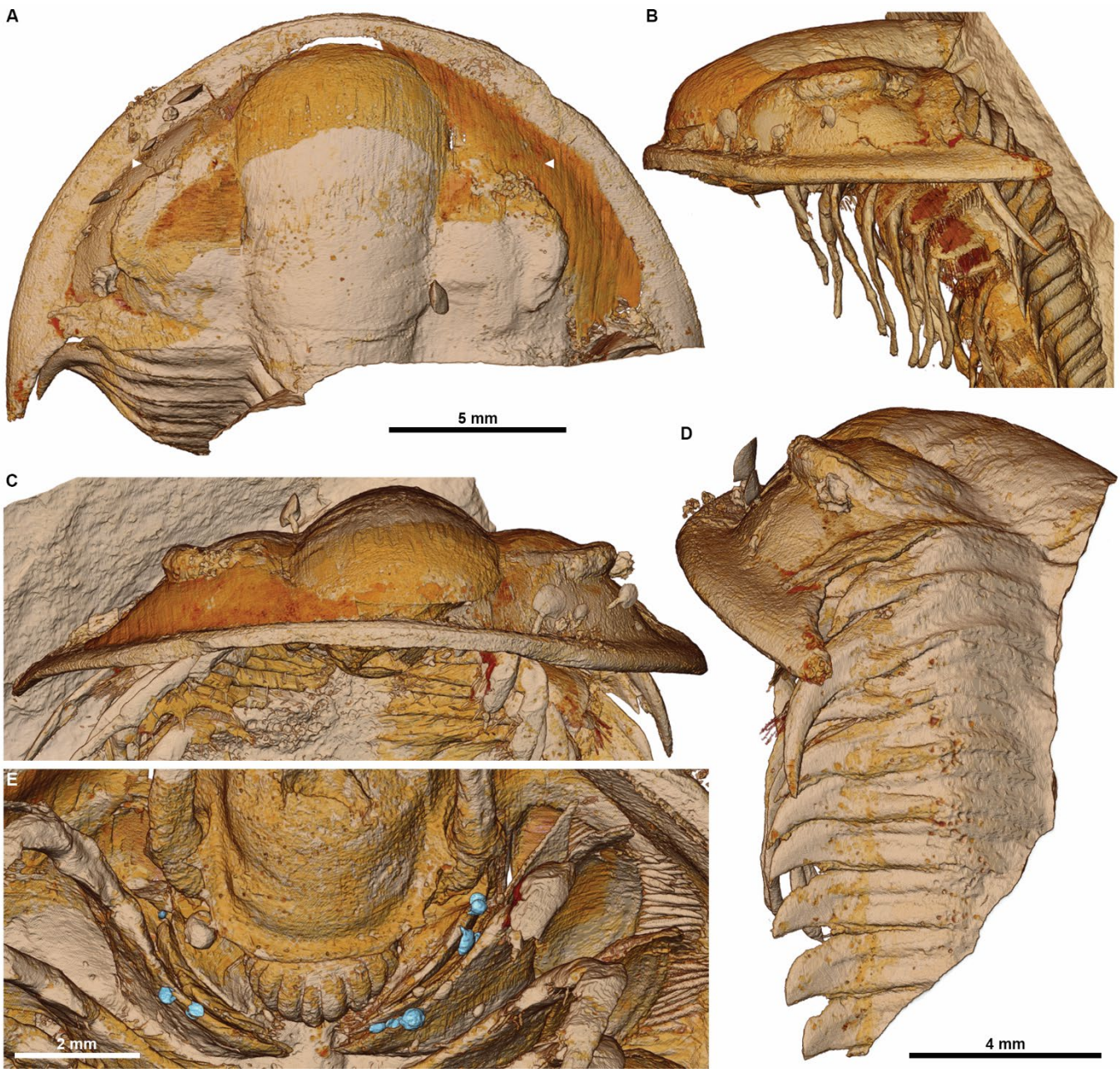

Fig. S5. External morphology of *Gigoutella mauretanica* (AY-TA-TB-02). (**A** to **C**) Dorsal, lateral and anterior views of partially enrolled individual showing details of dorsal exoskeleton, ventral appendages, and commensal brachiopods attached to the cephalon; white arrows in (A) indicate position of anterior facial sutures; scale bar for (A) also applies to (B and C). (**D**) Oblique lateral view of dorsal exoskeleton showing elongate pleural spine on second thoracic segment. (**E**) Ventral view of cephalon showing epibionts (blue), including brachiopods, attached to the first and second post-antennal appendages.

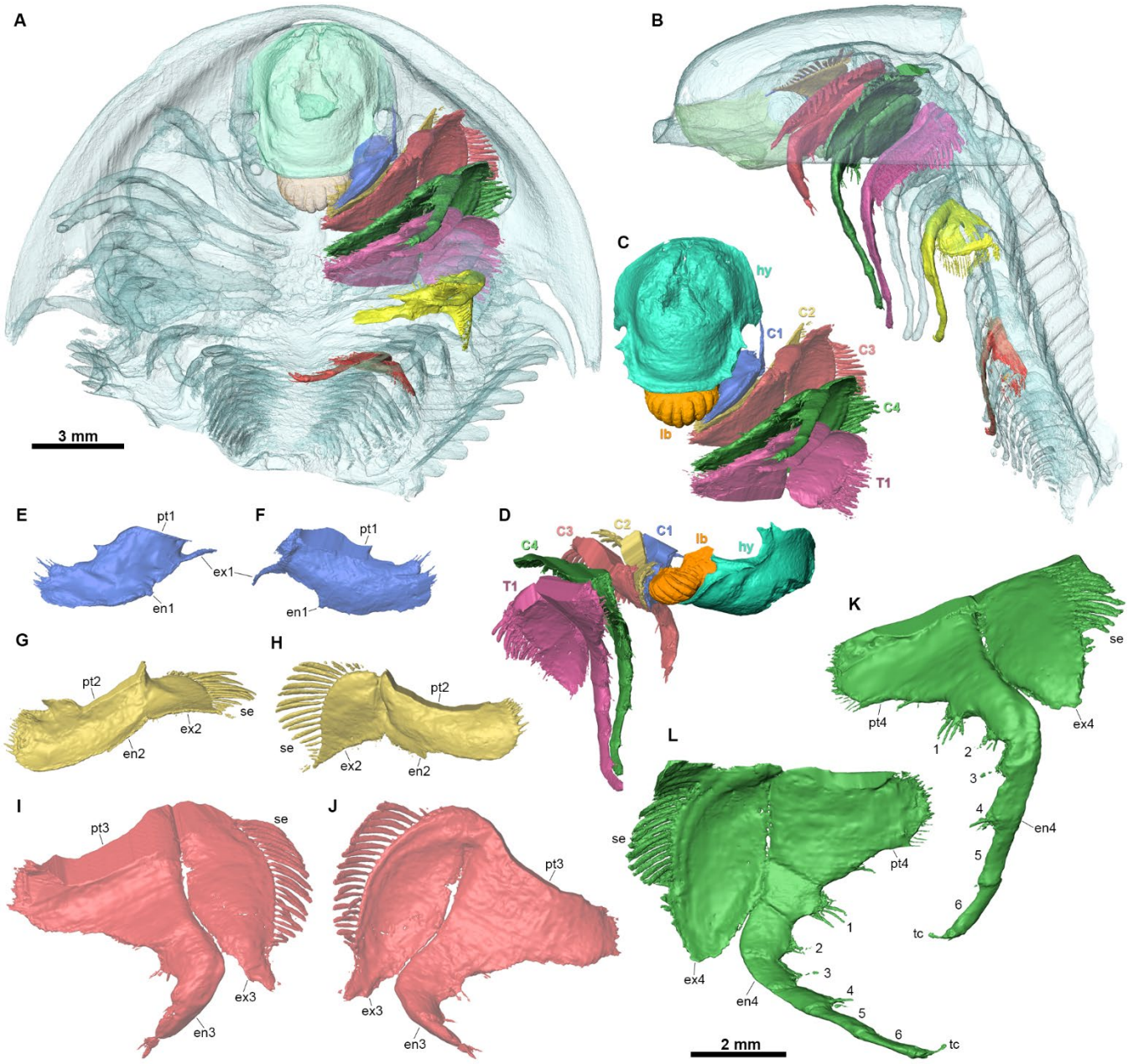

Fig. S6. Post-antennal appendages, hypostome and labrum of *Gigoutella mauretanica* (AY-TA-TB-02). (**A** and **B**) Ventral and lateral views, respectively, of partially enrolled individual showing the position of the post-antennal cephalic (C1–4; depicted in E to L) and thoracic (T1, T4, T8) appendages; (A) and (B) have surface rendering with transparency. (**C** and **D**) Ventral and sagittal views, respectively, of the cephalic (C1–4) and first thoracic (T1) appendages relative to the position of the hypostome and labrum. (**E** and **F**) Anterior and posterior views of C1 showing the protopodite, antenniform exopod, and rudimentary endopod. (**G** and **H**) Anterior and posterior views of C2 showing the protopodite, exopod with oblanceolate setae, and a rudimentary endopod. (**I** to **L**) Biramous appendages of the cephalon (C3 and C4) exhibiting a large protopodite, an endopod with seven podomeres (including terminal claws), and an exopod bearing oblanceolate setae. (I and J) Anterior and posterior views of C3. (K and L) Anterior and posterior views of C4. Scale bar for: (A) also applies to (B to D); (L) also applies to (E to K). C1–C4, cephalic (post-antennal) appendages 1–4; en*x*, endopod of *x*th post-antennal appendage (numerals 1–6 indicate endopodal podomeres); ex*n*, exopod of *n*th post-antennal appendage; hy, hypostome; lb, labrum; pt*n*, protopod of *n*th post-antennal appendage; se, setae; T1, first thoracic appendage; tc, terminal claw.

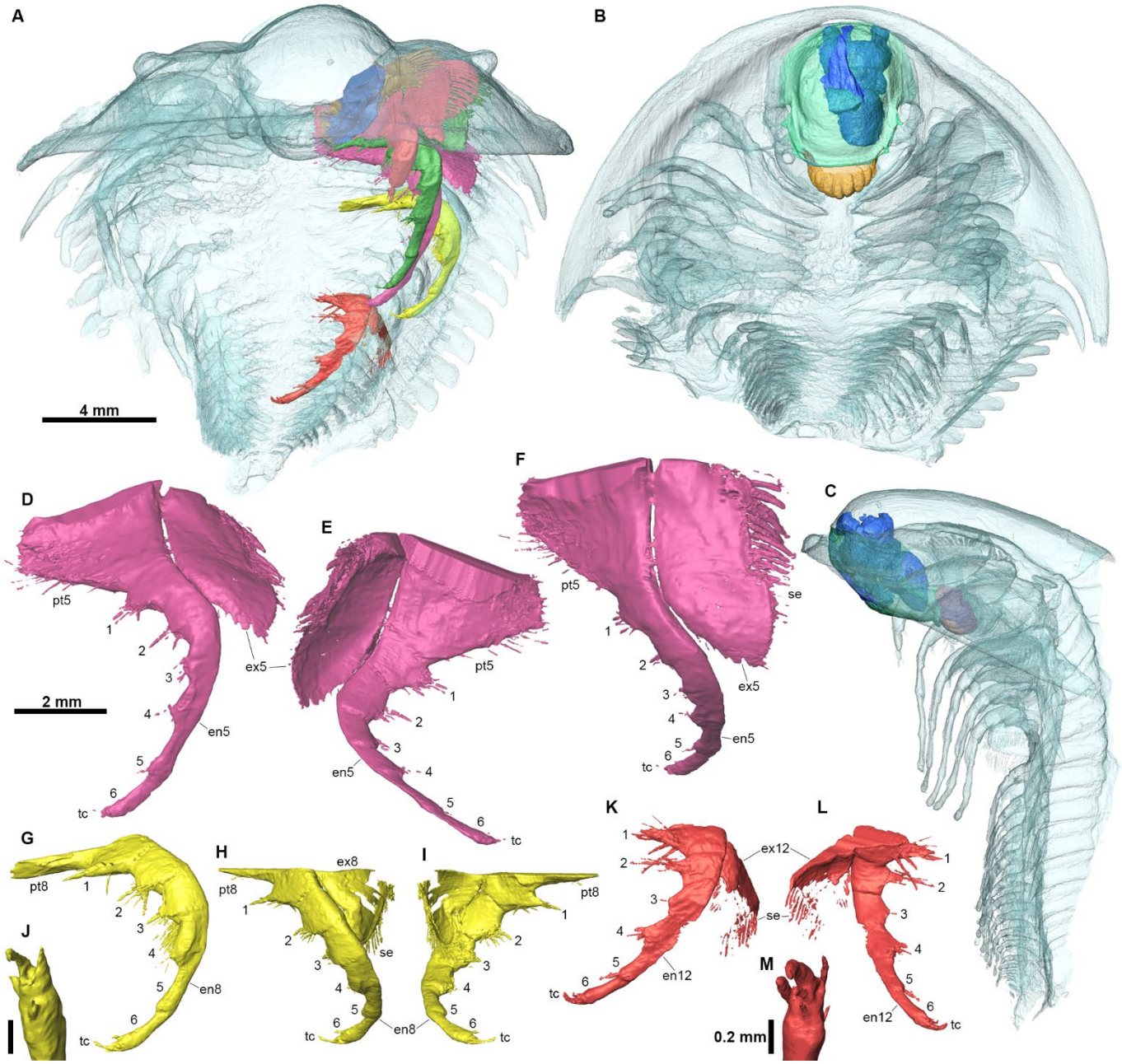

Fig. S7. Post-antennal appendages and crop of *Gigoutella mauretanica* (AY-TA-TB-02). (**A**) Ventral view showing the position of the post-antennal cephalic (C1–4) and thoracic (T1, T4, T8; depicted in D to M) appendages. (**B** and **C**) Ventral and lateral views, respectively, showing the hypostome (light green) and labrum (orange) *in situ*, and the collapsed crop of the digestive system (blue). (**D** to **M**) Biramous appendages of the thorax (T1, T4, T8) exhibiting the protopodite, an endopod with seven podomeres (including terminal claws), and an exopod bearing oblanceolate setae. (D to F) Anterior, posterior and oblique lateral views of T1. (G to J) Anterior, lateral, posterior views and close-up of terminal claws, respectively, of T4. (K to M) Anterior and posterior views and close-up of terminal claws, respectively, of T8. (A to C) have surface rendering with transparency. Scale bar for: (A) also applies to (B and C); (D) also applies to (E to I, K and L); (J and M) = 0.2 mm. en*x*, endopod of *x*th post-antennal appendage (numerals 1–6 indicate endopodal podomeres); ex*n*, exopod of *n*th post-antennal appendage; pt*n*, protopod of *n*th post-antennal appendage; se, setae; tc, terminal claws.

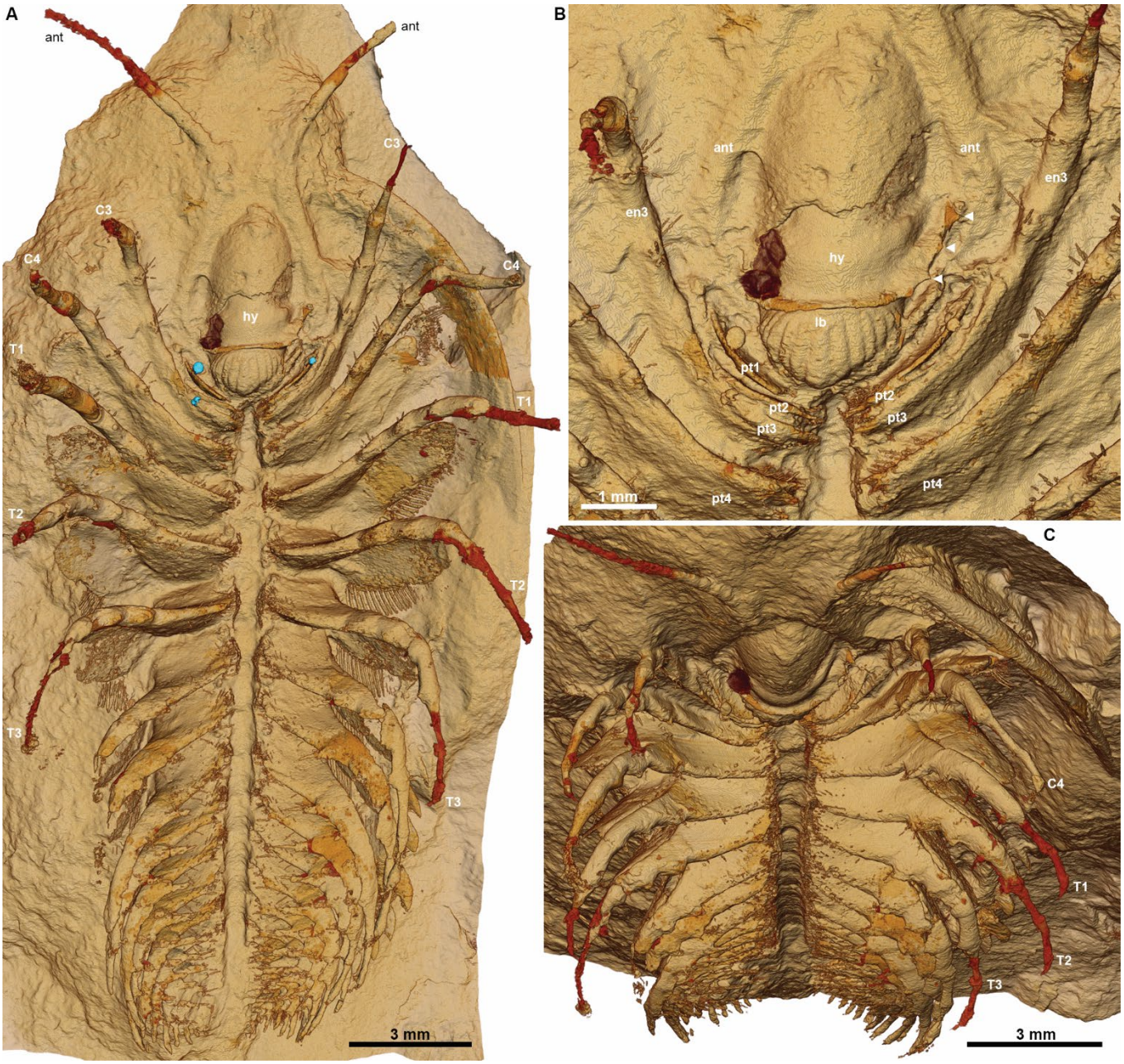

Fig. S8. External morphology of *Gigoutella mauretanica* (AY-TA-TB-01). (**A**) Ventral view showing paired appendages, the hypostome and labrum *in situ*, and commensal brachiopods (blue) attached to cephalic protopodites. (**B**) Close-up of ventral cephalic structures, including the antennae, hypostome bearing marginal spines (white arrows), labrum, and protopodites. (**C**) Oblique anteroventral view showing the deep axial food groove bounded by sternites and the gnathal edges of the protopodites. Volume is rendered based on an orange colour scale with light orange-beige colour for empty spaces and darker oranges for spaces filled by secondary minerals (e.g. distal portions of the antennae and endopods; note the dense mineral concretion on the hypostome). ant, antenna; C3, C4, cephalic (post-antennal) appendages 3 and 4; en3, endopod of 3rd post-antennal appendage; hy, hypostome; lb, labrum; pt*n*, protopod of *n*th post-antennal appendage; T1–T3, thoracic appendages 1–3.

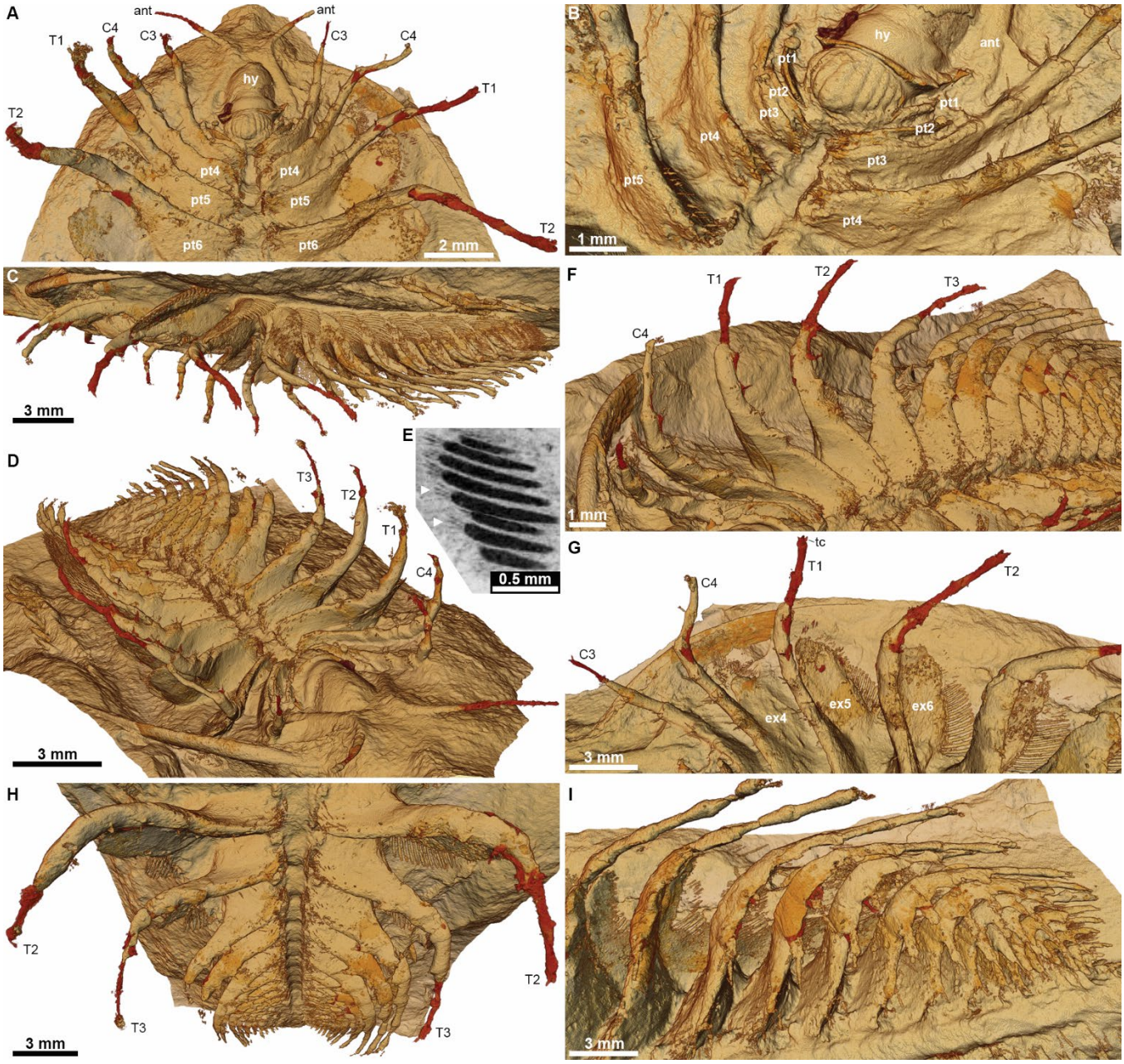

Fig. S9. External morphology of *Gigoutella mauretanica* (AY-TA-TB-01). (**A** and **B**) Oblique ventral views showing the arrangement of cephalic and anterior thoracic appendage pairs relative to the hypostome, labrum and food groove. (**C** and **D**) Lateral and oblique anteroventral views showing the relative positions of the protopodites, endopods and exopods in the post-antennal appendages. (**E**) Minimum-intensity projection of a 75-µm-thick ROI through the proximal exopod lobe setae on the seventh thoracic (T7) appendage; arrows indicate up to four bristle-like structures emerging from the apical ends of each seta. (**F** and **G**) Oblique ventral views showing details of the protopodites, endopods and exopods in the post-antennal appendages. (**H**) Oblique anteroventral view showing the axial food groove and details of the protopodites and endopods of the thoracic appendages. (**I**) Ventral view showing details of the posterior thoracic appendages, including endopods displaying endites that become progressively elongate posteriorly. ant, antenna; C3, C4, cephalic (post-antennal) appendages 3 and 4; ex*n*, exopod of *n*th post-antennal appendage; hy, hypostome; pt*n*, protopod of *n*th post-antennal appendage; T1–T3, thoracic appendages 1–3; tc, terminal claws.

	Sample	SiO_2 %	Al_2O_3 %	Fe_2O_3 %	MnO %	MgO %	CaO %	Na_2O %	K_2O %	TiO_2 %	P_2O_5 %	Th ppm	Sc ppm	La ppm	Th/Sc	La/Sc
Pyroclastic level (Tatelt Fm)	AY25.2	50,99	17,14	15,18	0,15	2,37	1,33	5,31	0,39	1,83	0,29	2,01	29,07	19,14	0,07	0,66
	AY25.1	60,20	13,96	12,28	0,13	1,83	1,04	4,52	0,19	1,54	0,35	1,25	18,39	10,13	0,07	0,55
	4	64,18	9,65	7,76	0,11	1,17	5,34	3,54	0,08	1,23	0,60	0,81	14,66	13,6	0,05	0,93
	3	64,80	11,56	9,25	0,11	1,40	2,49	4,11	0,12	1,30	0,42	1,05	15,06	10,0	0,07	0,66
	2	62,13	10,26	8,43	0,13	1,29	5,46	3,65	0,09	1,22	0,40	0,85	15,60	10,3	0,05	0,66
	1	63,98	9,11	7,44	0,12	1,14	6,33	3,32	0,08	1,16	0,58	0,75	14,40	13,6	0,05	0,94
	0A	48,05	14,10	13,69	0,27	2,11	6,60	4,47	0,10	1,45	0,18	0,82	22,59	8,95	0,04	0,40
Tatelt Formation	AY22	50,57	18,80	13,24	0,19	2,16	0,68	4,99	1,59	1,82	0,26	2,49	23,82	9,31	0,10	0,39
	AY21	51,94	15,36	11,35	0,17	1,88	4,51	5,37	0,34	1,55	0,32	2,59	15,69	14,09	0,17	0,90
	AY20	51,37	17,29	13,80	0,15	2,36	1,98	5,79	0,28	1,66	0,31	2,76	23,66	20,33	0,12	0,86
	AY19	55,50	17,46	10,84	0,16	1,85	1,06	6,76	0,42	1,33	0,33	1,82	18,50	9,66	0,10	0,52
	AY18	51,06	16,72	10,57	0,12	1,95	4,36	6,54	0,27	1,64	0,40	2,26	20,00	17,93	0,11	0,90
	AY17	57,45	15,10	9,47	0,11	1,64	2,81	5,81	0,27	1,39	0,88	2,62	16,79	23,91	0,16	1,42
	AY16.2	64,01	15,94	3,95	0,05	0,68	2,15	7,76	0,33	1,49	0,64	2,09	16,81	21,04	0,12	1,25
	AY16.1	60,25	15,65	5,11	0,07	0,91	3,91	7,28	0,27	1,35	0,86	2,07	16,94	33,16	0,12	1,96
	AY15	48,94	19,38	11,13	0,07	2,39	1,77	4,37	2,74	1,46	0,34	5,38	24,35	17,08	0,22	0,70
	AY14	54,48	17,11	12,21	0,09	2,33	1,39	5,22	0,94	1,64	0,20	2,32	20,52	8,14	0,11	0,40
	AY13	43,45	12,68	13,90	0,25	2,27	11,07	2,65	0,87	0,96	0,28	1,91	14,56	26,27	0,13	1,80
	AY12.2	50,24	15,08	17,17	0,15	2,96	2,94	2,98	0,94	1,40	0,54	6,13	17,38	21,98	0,35	1,26
	AY12.1	48,69	18,07	14,66	0,11	2,71	2,08	4,02	1,90	1,52	0,52	7,39	20,42	18,64	0,36	0,91
	AY11	50,91	17,62	14,17	0,13	2,84	2,04	4,34	1,70	1,43	0,46	2,24	17,13	15,53	0,13	0,91
	AY10	48,00	16,83	11,88	0,14	2,45	4,76	4,06	1,94	1,28	0,59	5,53	20,26	19,51	0,27	0,96
	AY9	38,78	16,99	17,93	0,31	3,29	5,05	2,51	1,61	1,70	1,99	5,82	33,99	63,99	0,17	1,88
	AY8	47,60	19,77	14,24	0,13	2,93	0,93	4,22	2,55	1,64	0,33	2,92	21,76	11,64	0,13	0,54
	AY7	70,88	13,54	4,00	0,07	0,79	0,59	5,07	1,32	0,81	0,23	3,82	9,41	24,78	0,41	2,63
	AY6.2	67,42	14,81	5,49	0,17	1,16	0,66	5,74	1,04	1,05	0,29	3,51	15,08	25,73	0,23	1,71
	AY6.1	71,78	13,41	3,57	0,09	0,76	0,51	5,24	1,09	0,69	0,19	3,37	12,62	16,25	0,27	1,29
	AY5	70,27	13,55	4,52	0,04	0,95	0,69	4,89	1,57	0,91	0,24	4,70	10,14	48,04	0,46	4,74
	AY4	48,66	19,81	12,89	0,22	2,47	1,13	4,25	3,09	1,02	0,40	2,52	19,81	17,19	0,13	0,87
	AY3	50,16	19,13	13,23	0,15	2,93	1,09	5,92	0,89	1,40	0,46	3,01	20,09	13,67	0,15	0,68
	AY2.2	66,53	16,52	3,20	0,13	0,87	0,80	7,75	0,59	1,31	0,33	3,34	14,94	22,84	0,22	1,53
	AY2.1	77,07	10,70	1,80	0,095	0,55	0,68	4,46	1,25	0,56	0,16	3,74	8,85	55,35	0,42	6,25
	AY1	59,98	16,66	8,34	0,072	2,34	0,55	2,23	3,57	0,64	0,17	5,22	12,82	14,16	0,41	1,10
	A-Ay28	66,79	12,71	4,81	0,058	1,34	2,24	4,10	1,92	0,81	0,23	4,61	8,95	34,0	0,51	3,80
	A-Ay27	64,42	14,33	7,02	0,071	1,95	1,25	3,90	1,96	0,90	0,21	4,76	8,06	31,1	0,59	3,86
	A-Ay25	62,43	15,58	8,16	0,087	3,14	0,39	2,42	3,29	0,60	0,14	5,62	12,59	27,9	0,45	2,22
	A-Ay23	39,93	16,73	12,59	0,29	4,14	8,87	3,18	1,84	0,94	0,14	1,69	17,80	15,9	0,09	0,89
	A-Ay22	61,41	17,00	6,79	0,067	2,99	0,43	2,09	4,25	0,75	0,17	8,01	17,20	30,6	0,47	1,78
	A-Ay19	68,18	13,45	6,77	0,069	2,48	0,33	2,79	2,47	0,45	0,12	4,08	8,50	35,4	0,48	4,17
	A-Ay18	62,99	13,94	6,78	0,098	2,03	2,48	4,26	1,54	0,95	0,22	3,83	11,04	24,2	0,35	2,19
	A-Ay15	63,64	15,11	7,71	0,073	2,70	0,44	2,52	3,07	0,74	0,17	5,75	12,38	62,1	0,46	5,01
	A-Ay12	65,98	14,59	6,88	0,063	2,59	0,41	2,59	2,92	0,63	0,17	6,10	11,92	51,3	0,51	4,31
	A-Ay10	63,24	15,64	6,88	0,063	2,74	0,75	2,24	3,56	0,73	0,17	6,76	13,82	47,6	0,49	3,44
	A-Ay9	62,96	15,95	6,59	0,066	2,76	0,74	2,35	3,74	0,77	0,19	5,96	13,82	39,7	0,43	2,87
	A-Ay3	61,87	15,68	6,36	0,043	2,18	1,55	2,07	3,76	0,71	0,16	5,76	13,17	39,7	0,44	3,02
	A-Ay2	61,99	12,70	4,24	0,082	1,51	4,50	3,73	2,12	0,70	0,16	3,42	8,83	16,2	0,39	1,83

Table S1. Whole-rock geochemical data from the Tatelt Formation section east of Ait Youb, Lemdad Syncline, High Atlas Mountains, Morocco.

Movie S1. MicroCT excursion of the dorsal and ventral morphologies of *Protolenus* (*Hupeolenus*) sp. specimen AY-TA-TB-03. The video first shows a scroll of microCT serial sections that reveals a volumetric rendering of the dorsal and ventral morphologies; a light orange-beige colour is used for the volumetric rendering of empty spaces, while darker orange represents the spaces filled by secondary minerals or concretions. It then focuses on the ventral anatomy, with surface rendering of the hypostome (green), labrum (red) and the post-antennal appendages C1–4, T1, T4, T8, with the rest of the body rendering with transparency.

Movie S2. MicroCT excursion of the appendages and digestive system of *Protolenus* (*Hupeolenus*) sp. specimen AY-TA-TB-03. The video shows a volumetric rendering of the appendages from a lateral perspective, then a ventral fly through of the deep axial food groove, followed by an exploration of the surface rendering of the digestive system (in blue). A light orange-beige colour is used for the volumetric rendering of empty spaces, while darker orange represents the spaces filled by secondary minerals or concretions. The surface rendering of the hypostome and labrum is green and red, respectively.

Movie S3. MicroCT excursion of *Gigoutella mauretanica* specimen AY-TA-TB-02. The video shows the virtual filling of void spaces within the rock. Then, a volume rendering of *Gigoutella mauretanica* appears, including the spaces filled by secondary minerals or concretions, shown in anterior, lateral and ventral views. It then focuses on the ventral anatomy, with surface rendering of the hypostome (green), the labrum (red) and the appendages C1–4, T1, T4, T8, with the rest of the body rendering with transparency. A light orange-beige colour is used for the volumetric rendering of empty spaces, while darker orange represents the spaces filled by secondary minerals or concretions; surface rendering of brachiopod epibionts is light blue.

Movie S4. MicroCT excursion of *Gigoutella mauretanica* specimen AY-TA-TB-01. The video shows the virtual filling of void spaces within the rock. Then, a volume rendering of *Gigoutella mauretanica* appears, shown in lateral and ventral views. A light orange-beige colour is used for the volumetric rendering of empty spaces, while darker orange represents the spaces filled by secondary minerals or concretions.

References and Notes

1. J. R. Paterson, The trouble with trilobites: Classification, phylogeny and the cryptogenesis problem. *Geol. Mag.* **157**, 35–46 (2020).

2. N. C. Hughes, A. Minelli, G. Fusco, The ontogeny of trilobite segmentation: A comparative approach. *Paleobiology* **32**, 602–627 (2006).

3. M. J. Hopkins, Development, trait evolution, and the evolution of development in trilobites. *Integr. Comp. Biol.* **57**, 488–498 (2017).

4. L. Laibl, F. Saleh, F. Pérez-Peris, Drifting with trilobites: The invasion of early post-embryonic trilobite stages to the pelagic realm. *Palaeogeogr. Palaeoclimatol. Palaeoecol.* **613**, 111403 (2023).

5. B. Schoenemann, An overview on trilobite eyes and their functioning. *Arthropod Struct. Dev.* **61**, 101032 (2021).

6. H. Zeng, F. Zhao, Z. Yin, M. Zhu, Appendages of an early Cambrian metadoxidid trilobite from Yunnan, SW China support mandibulate affinities of trilobites and artiopods. *Geol. Mag.* **154**, 1306–1328 (2017).

7. R. Lerosey-Aubril, T. A. Hegna, S. Olive, Inferring internal anatomy from the trilobite exoskeleton: The relationship between frontal auxiliary impressions and the digestive system. *Lethaia* **44**, 166–184 (2011).

8. H. B. Whittington, Trilobites with appendages from the Middle Cambrian, Burgess Shale, British Columbia. *Foss. Strata* **4**, 97–136 (1975).

9. S. R. Losso, J. Ortega-Hernández, Claspers in the mid-Cambrian *Olenoides serratus* indicate horseshoe crab-like mating in trilobites. *Geology* **50**, 897–901 (2022).

10. H. B. Whittington, J. E. Almond, Appendages and habits of the Upper Ordovician trilobite *Triarthrus eatoni*. *Philos. Trans. R. Soc. Lond. Ser. B* **317**, 1–46 (1987).

11. D. L. Bruton, W. Haas, The anatomy and functional morphology of *Phacops* (Trilobita) from the Hunsrück Slate (Devonian). *Palaeontographica Abt. A Paläozool. Stratigr.* **253**, 29–75 (1999).

12. Ú. Farrell, D. E. G. Briggs, R. R. Gaines, Paleoecology of the olenid trilobite *Triarthrus*: New evidence from Beecher's Trilobite Bed and other sites of pyritization. *Palaios* **26**, 730–742 (2011).

13. F. Pérez-Peris, L. Laibl, M. Vidal, A. C. Daley, Systematics, morphology, and appendages of an Early Ordovician pilekiine trilobite *Anacheirurus* from Fezouata Shale and the early diversification of Cheiruridae. *Acta Palaeontol. Pol.* **66**, 857–877 (2021).

14. R. Lerosey-Aubril, T. A. Hegna, C. Kier, E. Bonino, J. Habersetzer, M. Carré, Controls on gut phosphatisation: The trilobites from the Weeks Formation Lagerstätte (Cambrian; Utah). *PLOS ONE* **7**, e32934 (2012).

15. M. E. Eriksson, F. Terfelt, Exceptionally preserved Cambrian trilobite digestive system revealed in 3D by synchrotron-radiation X-ray tomographic microscopy. *PLOS ONE* **7**, e35625 (2012).

16. D. J. Siveter, R. A. Fortey, D. E. G. Briggs, D. J. Siveter, M. D. Sutton, The first Silurian trilobite with three-dimensionally preserved soft parts reveals novel appendage morphology. *Pap. Palaeontol.* **7**, 2245–2253 (2021).

17. C. E. Brett, T. E. Whiteley, P. A. Allison, E. L. Yochelson, The Walcott-Rust Quarry: Middle Ordovician trilobite Konservat-Lagerstätten. *J. Paleontol.* **73**, 288–305 (1999).

18. S. R. Losso, J. E. Thines, J. Ortega-Hernández, Taphonomy of non-biomineralized trilobite tissues preserved as calcite casts from the Ordovician Walcott-Rust Quarry, USA. *Commun. Earth Environ.* **4**, 330 (2023).

19. R. J. Ross, Jr., "Additional trilobites from the Ordovician of Kentucky" in "Contributions to the Ordovician paleontology of Kentucky and nearby states," J. Pojeta, Jr., Ed. (US Geological Survey Professional Paper 1066 A–G, US Government Printing Office, 1979), pp. D1–D13.

20. E. Landing, G. Geyer, W. Heldmaier, Distinguishing eustatic and epeirogenic controls on Lower–Middle Cambrian boundary successions in West Gondwana (Morocco and Iberia). *Sedimentology* **53**, 899–918 (2006).

21. J. J. Álvaro, F. Benziane, R. Thomas, G. J. Walsh, A. Yazidi, Neoproterozoic–Cambrian stratigraphic framework of the Anti-Atlas and Ouzellagh promontory (High Atlas), Morocco. *J. Afr. Earth Sci.* **98**, 19–33 (2014).

22. J. Ortega-Hernández, A. Azizi, T. W. Hearing, T. H. P. Harvey, G. D. Edgecombe, A. Hafid, K. El Hariri, A xandarellid artiopodan from Morocco - a middle Cambrian link between soft-bodied euarthropod communities in North Africa and South China. *Sci. Rep.* **7**, 42616 (2017).

23. R. S. Crawford, S. Casadío, R. M. Feldmann, M. Griffin, A. Parras, C. E. Schweitzer, Mass mortality of fossil decapods within the Monte León Formation (early Miocene), southern Argentina: Victims of Andean volcanism. *Ann. Carnegie Mus.* **77**, 259–287 (2008).

24. L. Elizalde, Volcanism and arthropods: A review. *Ecol. Austral* **24**, 1–132 (2014).

25. E. P. Maguire, R. M. Feldmann, S. Casadío, C. E. Schweitzer, Distal volcanic ash deposition as a cause for mass kills of marine invertebrates during the Miocene in northern Patagonia, Argentina. *Palaios* **31**, 577–591 (2016).

26. W. L. Taylor, C. E. Brett, Taphonomy and paleoecology of echinoderm Lagerstätten from the Silurian (Wenlockian) Rochester Shale. *Palaios* **11**, 118–140 (1996).

27. M. D. Sutton, D. E. G. Briggs, D. J. Siveter, D. J. Siveter, Silurian brachiopods with soft-tissue preservation. *Nature* **436**, 1013–1015 (2005).

28. T. P. Topper, L. E. Holmer, J.-B. Caron, Brachiopods hitching a ride: An early case of commensalism in the middle Cambrian Burgess Shale. *Sci. Rep.* **4**, 6704 (2014).

29. S. Duggen, N. Olgun, P. Croot, L. Hoffmann, H. Dietze, P. Delmelle, C. Teschner, The role of airborne volcanic ash for the surface ocean biogeochemical iron-cycle: A review. *Biogeosciences* **7**, 827–844 (2010).

30. P. Ayris, P. Delmelle, Volcanic and atmospheric controls on ash iron solubility: A review. *Phys. Chem. Earth* **45–46**, 103–112 (2011).

31. D. E. G. Briggs, A. J. Kear, Decay and mineralization of shrimps. *Palaios* **9**, 431–456 (1994).

32. D. Wall-Palmer, M. T. Jones, M. B. Hart, J. K. Fisher, C. W. Smart, D. J. Hembury, M. R. Palmer, G. R. Fones, Explosive volcanism as a cause for mass mortality of pteropods. *Mar. Geol.* **282**, 231–239 (2011).

33. M. Cobianchi, N. Mancin, C. Lupi, M. Bordiga, H. C. Bostock, Effects of oceanic circulation and volcanic ash-fall on calcite dissolution in bathyal sediments from the SW Pacific Ocean over the last 550 ka. *Palaeogeogr. Palaeoclimatol. Palaeoecol.* **429**, 72–82 (2015).

34. R. R. Gaines, D. E. G. Briggs, P. J. Orr, P. Van Roy, Preservation of giant anomalocaridids in silica-chlorite concretions from the Early Ordovician of Morocco. *Palaios* **27**, 317–325 (2012).

35. R. A. Fortey, Ontogeny, hypostome attachment and trilobite classification. *Palaeontology* **33**, 529–576 (1990).

36. G. E. Budd, The origin and evolution of the euarthropod labrum. *Arthropod Struct. Dev.* **62**, 101048 (2021).

37. G. Scholtz, G. D. Edgecombe, The evolution of arthropod heads: Reconciling morphological, developmental and palaeontological evidence. *Dev. Genes Evol.* **216**, 395–415 (2006).

38. C. Aria, F. Zhao, M. Zhu, Fuxianhuiids are mandibulates and share affinities with total-group Myriapoda. *J. Geol. Soc. London* **178**, jgs2020-246 (2021).

39. L. Størmer, Studies on trilobite morphology. Part III. The ventral cephalic structures with remarks on the zoological position of the trilobites. *Nor. Geol. Tidsskr.* **29**, 108–158 (1951).

40. J. L. Cisne, *Triarthrus eatoni* (Trilobita): Anatomy of its exoskeletal, skeletomuscular, and digestive systems. *Palaeontographica Americana* **9**, 95–142 (1981).

41. T. S. Park, Trilobite hypostome as a fusion of anterior sclerite and labrum. *Arthropod Struct. Dev.* **77**, 101308 (2023).

42. J. Ortega-Hernández, Homology of head sclerites in Burgess Shale euarthropods. *Curr. Biol.* **25**, 1625–1631 (2015).

43. J. Ortega-Hernández, Making sense of 'lower' and 'upper' stem-group Euarthropoda, with comments on the strict use of the name Arthropoda von Siebold, 1848. *Biol. Rev. Camb. Philos. Soc.* **91**, 255–273 (2016).

44. J. Ortega-Hernández, R. Janssen, G. E. Budd, Origin and evolution of the panarthropod head - A palaeobiological and developmental perspective. *Arthropod Struct. Dev.* **46**, 354–379 (2017).

45. T. A. Hegna, The function of forks: *Isotelus*-type hypostomes and trilobite feeding. *Lethaia* **43**, 411–419 (2010).

46. R. E. Snodgrass, The feeding organs of Arachnida, including mites and ticks. *Smithson. Misc. Collect.* **110**, 1–93 (1948).

47. C. E. Beecher, Further observations on the ventral structure of *Triarthrus*. *Am. Geol.* **15**, 91–100 (1895).

48. L. Størmer, Studies on trilobite morphology. Part I. The thoracic appendages and their phylogenetic significance. *Nor. Geol. Tidsskr.* **19**, 143–273 (1939).

49. R. A. Fortey, R. M. Owens, Feeding habits in trilobites. *Palaeontology* **42**, 429–465 (1999).

50. R. D. C. Bicknell, J. D. Holmes, G. D. Edgecombe, S. R. Losso, J. Ortega-Hernández, S. Wroe, J. R. Paterson, Biomechanical analyses of Cambrian euarthropod limbs reveal

their effectiveness in mastication and durophagy. *Proc. Biol. Sci.* **288**, 20202075 (2021).

51. K. J. Müller, D. Walossek, Morphology, ontogeny, and life habit of *Agnostus pisiformis* from the Upper Cambrian of Sweden. *Foss. Strata* **19**, 1–124 (1987).

52. J. Moysiuk, J.-B. Caron, Burgess Shale fossils shed light on the agnostid problem. *Proc. Biol. Sci.* **286**, 20182314 (2019).

53. R. Lerosey-Aubril, J. S. Peel, Gut evolution in early Cambrian trilobites and the origin of predation on infaunal macroinvertebrates: Evidence from muscle scars in *Mesolenellus*. *Palaeontology* **61**, 747–760 (2018).

54. M. J. Hopkins, F. Chen, S. Hu, Z. Zhang, The oldest known digestive system consisting of both paired digestive glands and a crop from exceptionally preserved trilobites of the Guanshan Biota (Early Cambrian, China). *PLOS ONE* **12**, e0184982 (2017).

55. P. Kraft, V. Vaškaninová, M. Mergl, P. Budil, O. Fatka, P. E. Ahlberg, Uniquely preserved gut contents illuminate trilobite palaeophysiology. *Nature* **622**, 545–551 (2023).

56. D. E. G. Briggs, A. J. Kear, Decay and preservation of polychaetes: Taphonomic thresholds in soft-bodied organisms. *Paleobiology* **19**, 107–135 (1993).

57. R. Lerosey-Aubril, J. R. Paterson, S. Gibb, B. D. E. Chatterton, Exceptionally-preserved late Cambrian fossils from the McKay Group (British Columbia, Canada) and the evolution of tagmosis in aglaspidid arthropods. *Gondwana Res.* **42**, 264–279 (2017).

58. D. J. Siveter, D. E. G. Briggs, D. J. Siveter, M. D. Sutton, The Herefordshire Lagerstätte: Fleshing out Silurian marine life. *J. Geol. Soc. London* **177**, 1–13 (2020).

59. P. J. Orr, D. E. G. Briggs, D. J. Siveter, D. J. Siveter, Three-dimensional preservation of a non-biomineralized arthropod in concretions in Silurian volcaniclastic rocks from Herefordshire, England. *J. Geol. Soc. London* **157**, 173–186 (2000).

60. F. Saleh, T. Clements, V. Perrier, A. C. Daley, J. B. Antcliffe, Variations in preservation of exceptional fossils within concretions. *Swiss J. Palaeontol.* **142**, 20 (2023).

61. G. W. Brindley, G. Brown, Eds., *Crystal Structures of Clay Minerals and Their X-Ray Identification* (Mineralogical Society, 1980).

62. D. M. Moore, R. C. Reynolds Jr., *X-Ray Diffraction and the Identification and Analysis of Clay Minerals* (Oxford Univ. Press, ed. 2, 1997).

63. N. Tribovillard, T. J. Algeo, T. Lyons, A. Riboulleau, Trace metals as paleoredox and paleoproductivity proxies: An update. *Chem. Geol.* **232**, 12–32 (2006).

64. G. Geyer, E. Landing, "Ediacaran–Cambrian depositional environments and stratigraphy of the western Atlas regions" (*Beringeria*, Special Issue 6, 2006), pp. 47–112.

65. J. J. Álvaro, S. Clausen, "Paleoenvironmental significance of Cambrian hiatal shell accumulations in an intracratonic aborted rift, Atlas Mountains, Morocco," in "Dynamics of Epeiric Seas," B.R. Pratt, C. Holmden, Eds. (Geological Association of Canada Special Paper 48, 2008), pp. 39–54.

66. I. Berrada, A. Fekkak, A. Jouhari, H. Ezzouhairi, H. Ouanaimi, M. El Houicha, H. El Hadi, Example of post-Ediacarian complex volcanism emplaced during the Cambrian rifting in the western High Atlas, Morocco: Geochemical study and geotectonic

significance. *Bulletin de l'Institut Scientifique Section Sciences de la Terre* **40**, 115–130 (2018).

67. A. Pouclet, H. El Hadi, J. J. Álvaro, J.-M. Bardintzeff, M. Benharref, A. Fekkak, Review of the Cambrian volcanic activity in Morocco: Geochemical fingerprints and geotectonic implications for the rifting of West Gondwana. *Int. J. Earth Sci.* **107**, 2101–2123 (2018).

68. G. Geyer, A comprehensive Cambrian correlation chart. *Episodes* **42**, 321–332 (2019).

69. G. Geyer, Die marokkanischen Ellipsocephalidae (Trilobita: Redlichiida). *Beringeria* **3**, 3–363 (1990).

70. G. Geyer, Intercontinental, trilobite-based correlation of the Moroccan early Middle Cambrian. *Can. J. Earth Sci.* **35**, 374–401 (1998).

71. F. A. Sundberg, G. Geyer, P. D. Kruse, L. B. Mccollum, T. V. Pegel, A. Żylińska, A. Y. Zhuravlev, International correlation of the Cambrian Series 2-3, Stages 4-5 boundary interval. *Australas. Palaeontol. Mem.* **49**, 83–124 (2016).

72. J. J. Álvaro, H. Ezzouhairi, N. A. Ayad, A. Charif, L. Popov, M. L. Ribeiro, Short-term episodes of carbonate productivity in a Cambrian uplifted rift shoulder of the Coastal Meseta, Morocco. *Gondwana Res.* **14**, 410–428 (2008).

73. J. E. I. Walch, *Die Naturgeschichte der Versteinerungen zur Erläuterung der Knorrischen Sammlung von Merkwürdigkeiten der Natur* (Paul Jonathan Felstecker, 1771).

74. R. Richter, *Handwörterbuch der Naturwissenschaften*, R. Dittler, G. Joos, E. Korschelt, G. Linek, F. Oltmanns, K. Schaum, Eds. (Gustav Fisher, 1932), pp. 840–864.

75. G. F. Matthew, Illustrations of the fauna of the St. John Group. No. 4.: On the smaller-eyed trilobites of Division I, with a few remarks on the species of the higher divisions of the group. *Canadian Record of Science* **2**, 357–363 (1887).

76. R. Richter, E. Richter, Zur Frage des Unter-Kambriums in Nordost-Spanien. *Senckenbergiana* **29**, 23–39 (1948).

77. S. R. Westrop, E. Landing, Lower Cambrian (Branchian) trilobites and biostratigraphy of the Hanford Brook Formation, southern New Brunswick. *J. Paleontol.* **74**, 858–878 (2000).

78. G. Geyer, E. Landing, A unified Lower-Middle Cambrian chronostratigraphy for West Gondwana. *Acta Geol. Pol.* **54**, 179–218 (2004).

79. T. Weidner, G. Geyer, J. O. R. Ebbestad, V. von Seckendorff, Glacial erratic boulders from Jutland, Denmark, feature an uppermost lower Cambrian fauna of the Lingulid Sandstone Member of Västergötland, Sweden. *Bull. Geol. Soc. Den.* **63**, 59–86 (2015).

80. P. Cederström, G. Geyer, P. Ahlberg, C. H. Nilsson, J. Ahlgren, Ellipsocephalid trilobites from Cambrian Series 2 and Stage 4, with emphasis on the taxonomy, morphological plasticity and biostratigraphic significance of ellipsocephalids from Scania, Sweden. *Foss. Strata* **67**, 1–131 (2022).

81. G. F. Matthew, *Protolenus* – a new genus of Cambrian trilobites. *Bulletin of the Natural History Society of New Brunswick* **10**, 34–37 (1892).

82. N. C. Hughes, Trilobite tagmosis and body patterning from morphological and developmental perspectives. *Integr. Comp. Biol.* **43**, 185–206 (2003).

83. W. Bednarczyk, H. Jurkiewicz, S. Orłowski, Lower Cambrian and its fauna from the Boring of Zaręby near Łagów (Holy Cross Mts). *Bull. Acad. Pol. Sci., Ser. Sci. Geol. Geogr.* **13**, 231–236 (1965).

84. J. J. Álvaro, E. Liñán, Nuevos datos acerca del Bilbiliense (Cámbrico Inferior terminal) en las Cadenas Ibéricas y su correlación con otras áreas. *Rev. Esp. Paleontol.* **12**, 277–280 (1997).

85. A. Żylińska, Z. Szczepanik, Trilobite and acritarch assemblages from the Lower–Middle Cambrian boundary interval in the Holy Cross Mountains (Poland). *Acta Geol. Pol.* **59**, 413–458 (2009).

86. G. Geyer, B. Buschmann, O. Elicki, A new lowermost middle Cambrian (Series 3, Stage 5) faunule from Saxony (Germany) and its bearing on the tectonostratigraphic history of the Saxothuringian domain. *Palaontol. Z.* **88**, 239–262 (2014).

87. P. R. Hupé, "Contribution à l'étude du Cambrien inférieur et du Précambrien III de l'Anti-Atlas Marocain" (Direction de la Production Industrielle et des Mines, Division des Mines et de la Géologie, Service Géologique, *Notes et Mémoires* 103, 1953), pp. 1–402.

88. K. Sdzuy, in *Memorias de las IV Jornadas Aragonesas de Paleontología: La expansión de la vida en el Cámbrico. Libro homenaje al Prof. Klaus Sdzuy*, J. Gámez-Vintaned, E. Liñán, Eds. (Institución Fernando el Católico, 1995), pp. 253–263.

89. W.-T. Zhang, Y. Lu, Z. Zhu, Y. Qian, H. Lin, Z. Zhou, S. Zhang, J. Yuan, Cambrian trilobite faunas of southwestern China. *Palaeontologia Sinica* **159**, 1–497 (1980).

90. H. Luo *et al.*, *Early Cambrian Malong Fauna and Guanshan Fauna from Eastern Yunnan* (Yunnan Science and Technology Press, 2008).

91. T.-R. Lin, S.-C. Peng, New material of *Palaeolenus* (Trilobite, Cambrian) from the eastern Yangtze Gorge area, western Hubei. *Acta Palaeontologica Sin.* **43**, 32–42 (2004).

92. R. Gozalo, E. Liñán, M. E. Dies Álvarez, J. A. Gámez Vintaned, E. Mayoral, *The Evolution of the Rheic Ocean: From Avalonian-Cadomian Active Margin to Alleghenian-Variscan Collision*, U. Linnemann, R. D. Nance, P. Kraft, G. Zulauf, Eds. (Geological Society of America, 2007), pp. 359–373.

93. O. Elicki, G. Geyer, The Cambrian trilobites of Jordan – taxonomy, systematic and stratigraphic significance. *Acta Geol. Pol.* **63**, 1–56 (2013).